Prediction of Friction Stir Welding effects on AA2024-T3 plates and stiffened panels using a shell-based finite element model

Prediction of Friction Stir Welding effects on AA2024-T3 plates and stiffened panels using a shell-based finite element model

R.M.F. Paulo[1], P. Carlone[2], V. Paradiso[2], R.A.F. Valente[1,a], F. Teixeira-Dias[3],

[1]GRIDS Research Group, Department of Mechanical Engineering, University of Aveiro, Portugal

[2]Department of Industrial Engineering, University of Salerno, Italy

[3]Institute for Infrastructure and Environment, School of Engineering, The University of Edinburgh, United Kingdom

[a] *Corresponding author: robertt@ua.pt (Robertt Valente)*

Abstract (max. 100):

Manufacturing-induced effects can strongly affect in-service behaviour of welded structures, such as integrally stiffened panels for aeronautic applications. Being a complex phenomenon with several variables involved, the assessment of effects coming from welding usually relies on numerical simulations. Here, a novel shell-based finite element model is proposed to accurately simulate transient thermal fields and stress-strain distributions resulting from friction stir welding (FSW) processes. It is shown that the proposed model is able to accurately predict the (i) residual stresses; (ii) material softening and (iii) geometric distortion effects, in an comprehensive way, of friction stir welded aluminium integrally stiffened panels.

Keywords (max. 6):

AA2024-T3; Friction Stir Welding; Shell finite elements; Residual stresses; Distortion; Stiffened panels.

1. Introduction

Stiffened panels are the common choice for structural elements subjected to bending and buckling loads in several demanding applications with high strength/weight ratio, such as airplane wings and fuselages. By a proper choice of material and geometric parameters (particularly the cross sectional dimensions), these structures can withstand complex load scenarios. Loading patterns can derive from combinations of longitudinal compressive (buckling), transverse and in-plane shear forces, together with those perpendicular to the base plate (bending effects) [1]. For this reason, modelling and prediction of geometric deviations are of crucial importance, particularly those coming from joining operations of individual panels.

The use of friction stir welding (FSW) to join stiffened panels has recently been investigated as an alternative of other joining techniques, such as riveting or fusion welding processes [2]-[4]. FSW is a well-established solid state welding process that enables to efficiently weld almost all types of aluminium alloys, even those traditionally classified as non-weldable by fusion welding means [5]. Although residual stresses and geometric distortion coming from FSW processes are lower compared to other joining processes, the impact of such effects on performances of welded structures must be carefully assessed [6]-[8].

In this study, modelling and numerical analyses of FSW processes were performed using the FEM software package Abaqus [9]. One of the main characteristics of the proposed numerical finite element framework is that the parts to be welded were modelled exclusively using shell finite elements. Although shell elements have been tested by different authors [10]-[12], solid (continuum) elements are most widespread in the literature [13]-[15]. Despite this, shell elements make the meshing process simpler and faster, relying on a single reference surface where nodes are located (typically, the neutral surface). In terms of analysis, shell elements allow lower computational times, mainly due to the lower number of elements to be used in the model. Moreover, shells allow

for a more straightforward discretization of thin-walled structures, at the same time avoiding over-stiffness effects coming from transverse shear locking [16].

Plate and shell structures are often reinforced with slender stiffeners, increasing the load-carrying capacity of the structures without giving up their lightweight property. To this purpose, numerical modelling is of fundamental importance in understanding FSW effects on structural behaviour of stiffened panels to avoid conservative design choices, often motivated by an attempt to compensate for structural analysis uncertainties.

In the present work, a 3-stage modelling/numerical procedure is proposed for the coupled thermo-mechanical, quasi-static, analysis. In the first stage, a heat source moves along the weld line. On the second stage, a cooling step of the joined structure is enforced. During these two initial stages, mechanical boundary conditions are applied to simulate the clamping system. The third stage of the simulation corresponds to the release of the joined structure from the supports, where the boundary conditions are replaced by minimal constrains to prevent rigid body movements. No remeshing procedures were needed to reduce the involved computational costs, which is a distinguish feature of the proposed procedure. Temperature dependence of relevant material parameters was accounted for to ensure a reliable numerical simulation procedure. Also, thermal softening is considered, not only as temperature dependent but also as temperature-history dependent, which is another distinctive feature of the present approach. Pioneering work in this was conducted by Sonne [17], which assessed that the microstructural evolution of the material during FSW is expected to have a considerable effect on the residual stress distribution. Experimental work was also conducted by Genevois et al. [18], to demonstrate that during the thermal cycle of welding, dissolution, precipitation and coarsening occur in the heat and and thermomechanical affected zone (HAZ/TMAZ). This results in softening of the material, with a consequent reduction of the yield strength, and these effects can be successfully predicted with the proposed numerical model. Although brick and tetrahedral elements have been used [19],[20] to account for

dissolution/precipitation in precipitation hardened aluminium alloys, the shell-based methodology proposed in this study proves to be an straightforward and robust modelling option with lower computational costs.

The proposed models are first calibrated in the simulation of a relatively simple benchmark consisting of single plates joining, being subsequently validated using reference experimental data, obtained by authors in previous papers [21]-[23]. Doing so, AA2024-T3 plates were friction stir welded using a HSS unthreaded tool and subsequently microstructurally and mechanically characterized [22]. The residual stress levels coming from the joining process were inferred by the contour method [24], following the hybrid numerical–experimental procedure reported in [23]. The validated model was afterwards applied to simulate FSW process of stiffened panels for aeronautical applications.

2. Materials and Methods

A model of the welded plate, with the same dimensions of the one used in the experiments [25], was discretized using shell elements. A sensitivity study was carried out on the proper mesh density needed, the type of shell element to be chosen and the optimum number of integration point across thickness, seeking for a reasonable calculation time without compromising the accuracy of the results. Different types of heat source distribution were tested and the sensitivity of the numerical model to distinct mechanical boundary conditions (simulating the clamping system) was also assessed. Details concerning material modelling, element formulation, discretization, boundary and loading conditions are detailed presented in the following sections.

2.1 Material modelling

In the present work, thermal and mechanical properties of AA2024-T3 were defined following previous references [17],[22],[26]. Thermal conductivity, thermal expansion coefficient, specific heat capacity, Young's modulus and yield stress were considered as being temperature dependent,

and density and Poisson's ratio were assumed as temperature independent. An isotropic material model was applied for all the parameters. The material was considered to behave as perfectly plastic and therefore no hardening law was defined in the constitutive model [27].

Thermal softening effects were also considered, including a softening model to account for effects of temperature and temperature history on yield stresses. Among others, Sonne *et al.* [17] showed that the use of a softening model can lead to important changes in the prediction of residual stresses, compared to the solely use of temperature dependent material properties [17],[28]-[33]. In this regard, a softening model following Myrh and Grong [34] was assumed. The yield stress (σ) can the be defined by [17],[33]

$$\sigma = (\sigma_{\max} - \sigma_{\min})(1 - X_d) + \sigma_{\min}, \quad (1)$$

where $\sigma_{\max}$ is the yield stress of the material in the T3 condition, $\sigma_{\min}$ is the yield stress in the fully softened state and X_d is a dissolved precipitates fraction:

$$X_d = \sqrt{t_{eq}}. \quad (2)$$

In the equation, t_{eq} is given by:

$$t_{eq} = \sum_{i=1}^{N_{total}} \frac{\Delta t_i}{t_{ref}\, exp\left[\frac{Q_{ref}}{R}\left(\frac{1}{T_i} - \frac{1}{T_{ref}}\right)\right]}, \quad (3)$$

where Δt_i is the increment size (time), T_i is the current temperature, t_{ref} is the time for total dissolution at the reference temperature (T_{ref}), R is the universal gas constant and Q_{ref} is the effective activation energy for the dissolution of precipitates [17].

For every increment during the simulation, the parameter X_d is calculated and updated at each integration point, starting from 0 (material in the T3 condition) and ranging up to 1 (fully softened material), by means of an USDFLD user subroutine [9]. Yield stresses values are then obtained by an interpolation between upper ($\sigma_{\max}$) and lower ($\sigma_{\min}$) bounds of the yield stress values (equation

(1)). In particular for the lower bound curve, the values presented by distinct authors [17],[30] can be quite different. The curve presented in Figure 1 was then plotted based on a general pattern of variation with temperature from the available information and assuming a yield stress, at room temperature, of 205 MPa. This magnitude corresponds to 60% of the yield stress of the base material, being within the range of values in the literature [17],[27],[30]. The upper curve was plotted following a similar procedure, although the differences from distinct references were much smaller. The maximum yield stress at room temperature was set as 345 MPa [17],[27],[30],[35]. Figure 1 shows the evolution of yield stresses in a point of the plate during heating and cooling phases of the FSW process.

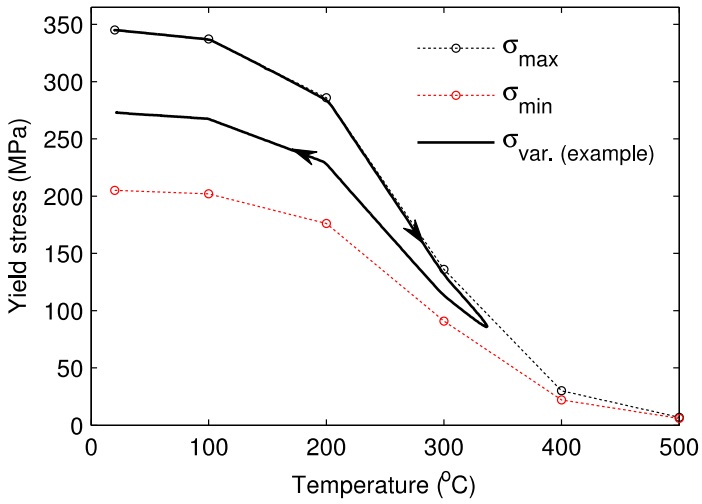

Figure 1: Yield stress curves used in the softening model, and an example of the yield stress variation during FSW processes.

2.2 Model discretization

Two types of shell elements from Abaqus library was tested: S4RT and S4T. These are 4-nodes thermo-mechanical coupled elements, with reduced (S4RT) and full (S4T) integration rules [9]. Two different numbers of integration points along thickness were tested for S4RT elements (5 and 9 points), with 5 integration points being chosen for S4T. Preliminary results for S4T shells showed that no advantages are obtained with a higher number of integration points along thickness for that

formulation. Three different mesh refinement levels with 0.5, 1, and 2 mm width were tested, all of them composed by square elements. A preliminary analysis also showed that the use of regular meshes with the adequate size led to a good quality of results, with no need for remeshing procedures. Results of sensitivity analyses showed that the use of full integration elements (S4T) instead of reduced integration (S4RT), or the use of more than 5 integration points across thickness, did not lead to significant differences in the results. Consequently, the combination of the S4RT formulation with 5 integration points across thickness, having a lower computational time, was chosen in the subsequent simulations, with a mesh size of 0.5 mm.

2.3 Loading and boundary conditions

FSW numerical analyses included the three different steps shown in Table 1, with the corresponding computational costs (% of the total CPU cost). Mechanical and thermal boundary conditions can vary from step to step, following what happens in experiment and represented in Figure 2. After welding, a last step was added to simulate the effects of ageing of the aluminium alloy, corresponding to an increase in the yield stress [36]-[38].

Table 1: FSW simulation steps, with the relative computational effort.

Step	Action	CPU time effort (%)
1	Tool passage (heat input)	72.2%
2	Cooling	26.8%
3	Clamping system release	0.5%
Extra stage	Ageing	0.5%

Concerning the mechanical boundary conditions, mechanical loads coming from contact conditions were not considered in the numerical model, since their influence is small compared to the thermal loads involved [30]. The current model presents a symmetry plane (in the weld line) in terms of

geometry, loading conditions and boundary conditions, therefore only half of the assembly (one of the parts to be welded) was modelled, with obvious benefits in the total computational time. Therefore, Figure 2 shows the FEM model of the friction stir butt welding of a couple of single plates where the nodes in the weld line were considered to have a symmetry boundary condition on the *Oyz* plane.

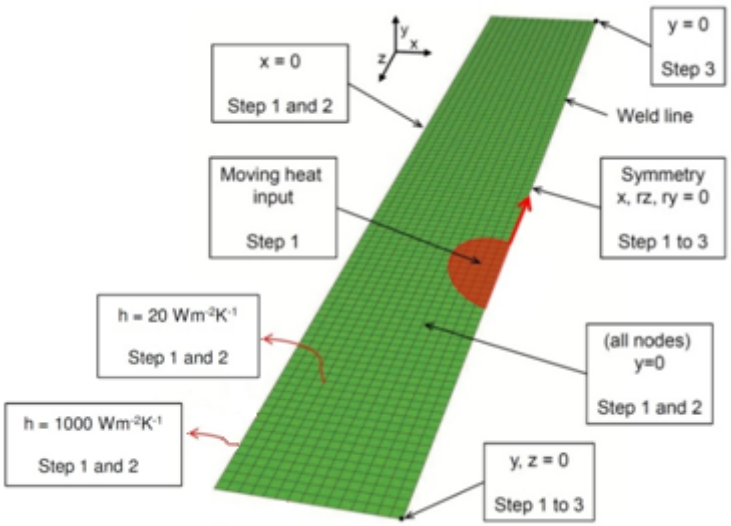

Figure 2: Boundary conditions (just half of the plate is shown, due to symmetry) [21].

About the clamping system, the models use constrains in the displacement/rotations in some sets of nodes [17],[29],[35], avoiding the cumbersome treatment of contact conditions in these areas and following previous works of the authors [21]. However, the results from [21] showed a high sensitivity of the numerical results to the mechanical boundary conditions used to model the clamping system. This can be related to the small width of the plate and consequent proximity of the displacement-restricted edge to the welded zone. The same sensitivity to boundary conditions was also inferred other authors [29].

Following Figure 2, in steps 1 and 2 (when the clamping system is present) displacements normal to the plate surface (*Oy* direction) were restricted, reproducing the effects of the base support and the

compression forces from the clamps. The displacement of nodes along the edge opposite to the weld line was also constrained in *Ox* direction (in the first two steps), reproducing the effects of the clamping system [24]. In step 3 of the simulation the boundary conditions related to the clamping are removed and a minimal set of constraints (to avoid rigid body movements) is applied to the model.

In terms of thermal boundary conditions, the heat transfer modelling (in and out) during the first two steps of the simulation was performed according to information provided in the literature, considering the dimensions of the adopted tool. In step 3 of the numerical analyses, which occurs after the cooling of the plate, no heat transfer was considered. During the first two steps, the heat flux output was modelled using distinct effective heat transfer coefficients for the top and for the bottom of the plate, following the equation:

$$q = -h(T - T^0), \quad (4)$$

where q is the heat flux across the surfaces, h is the heat transfer coefficient, T is the current temperature at the analysed point, and T^0 is the room temperature, which was set to 20º C. On the bottom surface of the plate, the heat transfer coefficient (h), related to the heat transfer between the plate and the steel base, was assumed to be 1000 $Wm^{-2}K^{-1}$, according to references in which similar analyses were performed [17],[39],[40]. At the top, the heat transfer coefficient (h) was set to 20 $Wm^{-2}K^{-1}$, accounting for convection heat transfer to the surrounding air [17],[40] and for some heat losses through the clamps. The time step for the cooling stage and the total heat input provided by the tool follow from previous experimental analysis [21], where a good agreement was found using a total power (Q) of 1300 W. Also in [21], different heat input distributions were tested, being concluded that variations in this parameter does not seem to have a significant influence on stress and softening results. Considering these conclusions, a simple distribution [35] was used and resembling a “pinless” tool, where the heat input variation along the radius (r) follows the equation:

$$q(r) = \frac{3Qr}{2\pi(R_1^3 - R_0^3)}. \quad (5)$$

This equation was used for the heat input on the top surface of the plate, with R_0 and R_1 corresponding to the center (0) and shoulder limit (10 mm), respectively. The heat flux distribution was implemented a user subroutine DFLUX [9], also responsible to define the position of the heat source advancing along the weld line.

In the following section, a detailed description of the numerical results is presented for the single plates joining model, where a subsequent validation is conducted using reference experimental data following the hybrid numerical–experimental procedure. The validated model was afterwards applied to simulate the whole FSW process of stiffened panels, aiming to predict the welding effects on the structural behaviour.

3. Results and discussion

3.1 Plate FSW process model

In this section, the simulation of the FSW process of two AA2024-T3 plates with 194 × 30 × 4 mm^3 is presented. The experimental trial is fully described in [24] and the simulation parameters were defined in accordance to this reference. In what follows, the data concerning the mapping of the full plate are relative to the top surface, where higher temperatures were achieved and the softening effect is more intense. As a reference to a better understanding of the results, the tool took 72.9 s to travel until the mid-length of the plate.

3.1.1 Softening and yield stress evolutions during FSW

The temperature evolution during the FSW process is responsible for variations on the softening value and the yield stress, represented in Figure 3 and Figure 4, respectively. From the results in Figure 3 it becomes evident that different temperature histories, being dependent on the distance

from the welding line, can lead to distinct evolutions in the material softening. The minimum value of softening (0.0) can be found at the welding line, along most of the panel length after the welding. Along points that are at a distance more than 15 mm from the welding line, the values are in the meanwhile always higher than 0.45. Results given in Figure 4 give a clear idea that the yield stress magnitude is a result of combined effects of the temperature and of the temperature history (through the softening magnitude). In the end of the cooling stage, when the temperature of the plate is equal to the room temperature, a similar pattern in the distribution of the material softening and yield stress can be seen, since in this moment the yield stress is only dependent on the temperature history.

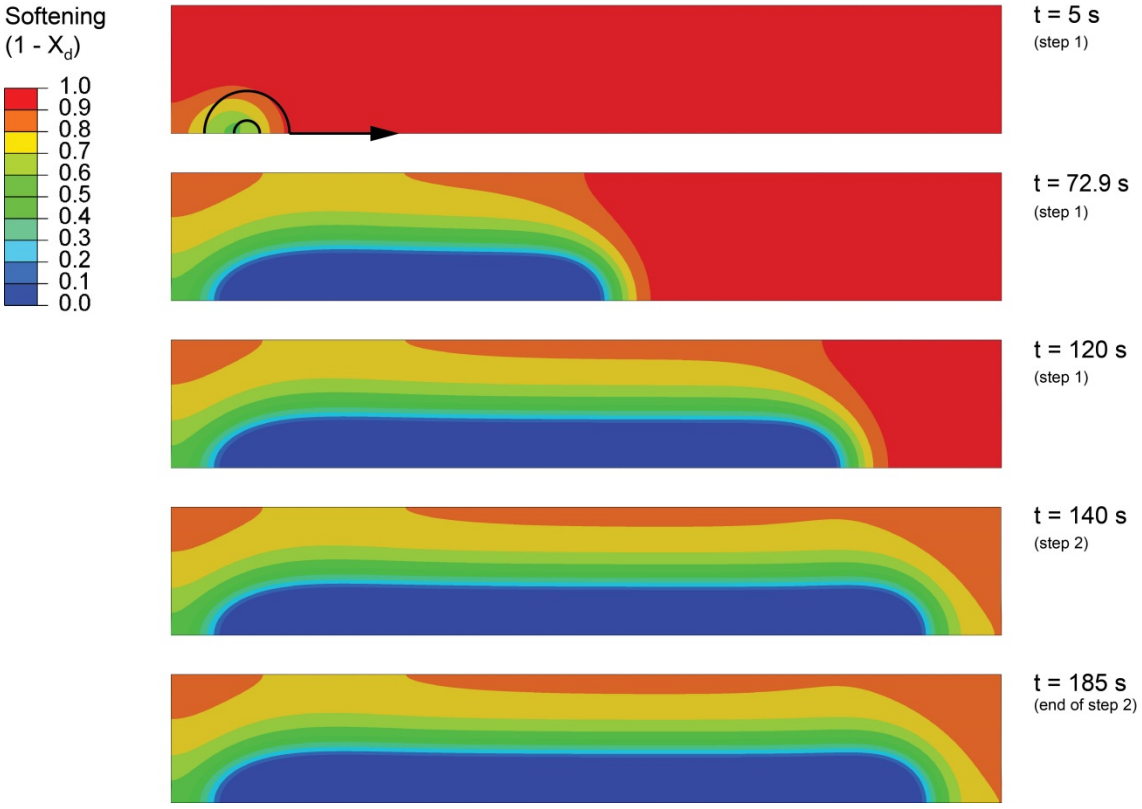

Figure 3: Evolution of material softening during the FSW analysis on the plate.

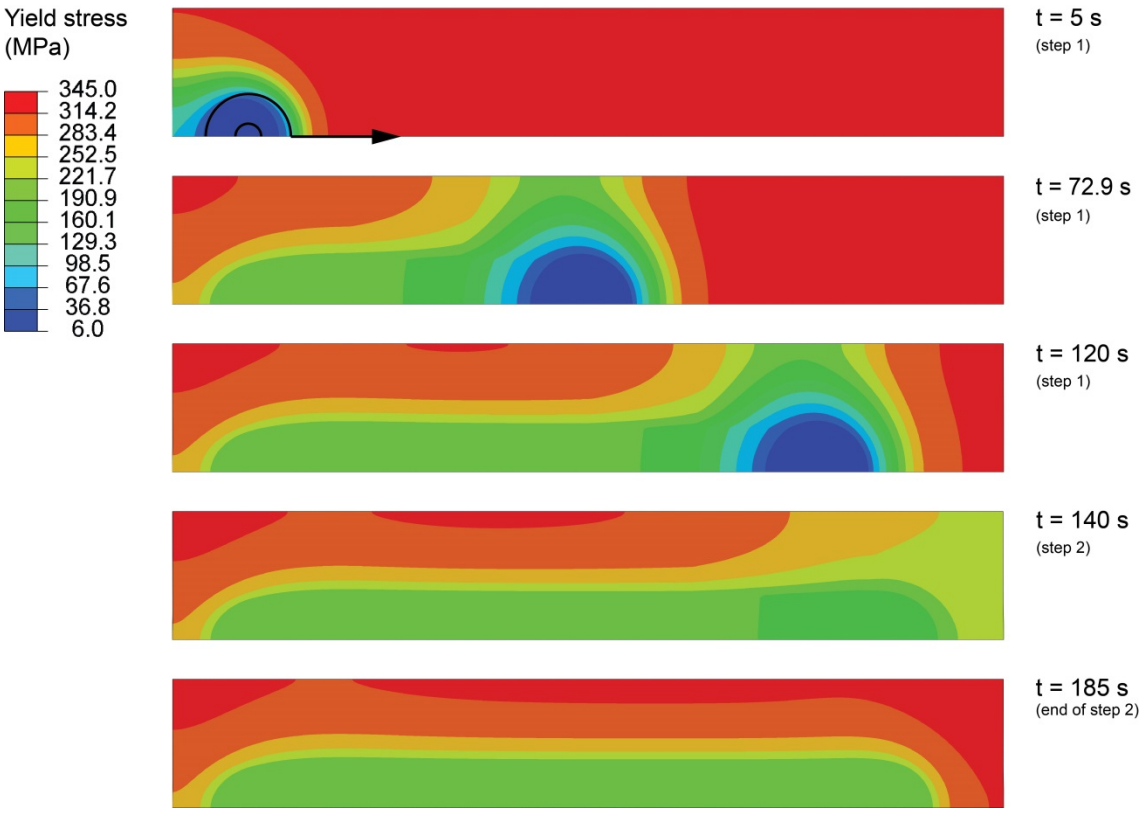

Figure 4: Yield stress evolution during the FSW analysis on the plate.

3.1.2 Ageing effects

It is well known that for AA2024 natural ageing occurs after a welding thermal cycle, and the re-precipitation process leads to a general improvement in mechanical properties, namely hardness and yield stress. To include the ageing effects in the hardness profile a simple methodology has been applied.

First, hardness distributions at the end of the welding process was inferred with the model previously used to calculate the yield stress (equation (1)) [17],[33], and hardness magnitudes were assumed to be in the form

$$HV = (HV_{max} - HV_{min})(1 - X_d) + HV_{min}\,, \qquad (6)$$

where HV_{max} and HV_{min} were defined as 156 and 93 HV, respectively, considering the experimental data in [22]. Using equation (6), the hardness in the mid-thickness of the mid-length section, at the end of the FSW simulation, can be calculated using the softening values. The results are plotted in

Figure 5 (solid red line) along with the experimental data. The experimentally measured hardness profile exhibits higher values than those obtained from the numerical model, especially along the (-16, 16) mm interval. This occurrence was obviously attributed to some ageing effects. In this work, the mechanical properties recovery was simulated assuming a 40% increase of the X_d factor, considering the experimental micro-hardness profile and then used to adjust also the yield stress distribution [22]. This second curve can be seen in Figure 5 (solid blue line).

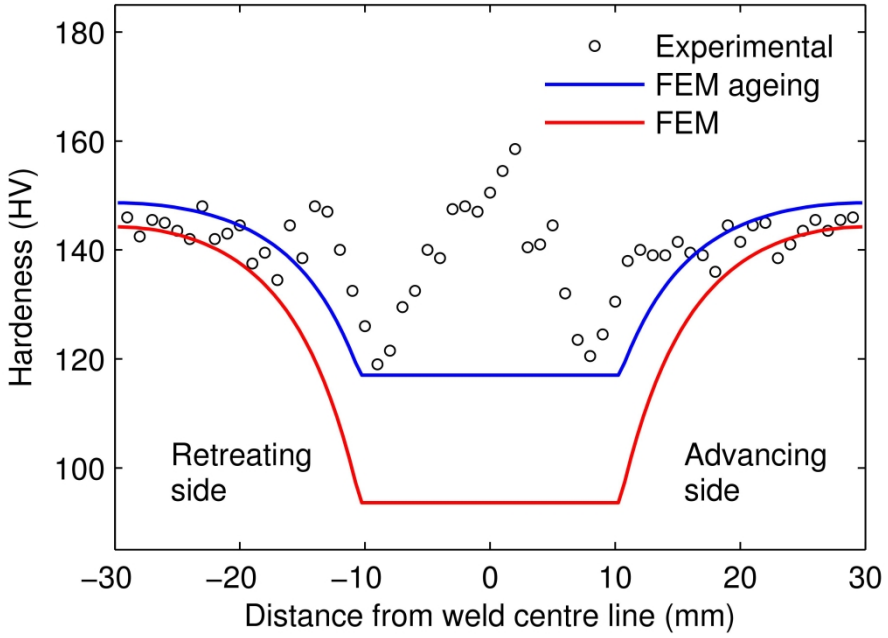

Figure 5: Comparison of the experimental hardness magnitude with the results obtained with the FEM model, before and after consideration of ageing effects [21].

The ageing evolution follows what is usually verified in experimental measurements, with a higher increase of hardness in the zone close to the weld line, and a lower increase in the zone where the material is less affected by welding [36]. It is worth noting the reliable prediction of the width of the HAZ, dictated by the micro-hardness variations. Obviously, this is not the case for the Nugget Zone (NZ) and Thermo-Mechanical Affected Zone (TMAZ) since the present models does not yet account for the local effects dominant in these areas [21].

3.1.3 Longitudinal and transverse stress evolution during FSW

The distribution of longitudinal stresses during and after the FSW process, along with the distribution of transverse stresses at the end of the process itself, is shown in Figure 6. Variations can be seen during welding of the longitudinal and transverse stresses in three points in the mid-length of the plate: P1, P2 and P3 (located at 5, 15 and 25 mm from the weld line). A compressive peak occurred at point P1 before the heat source passed by, from the thermal expansion in a position prior to this point. When the heat source got closer to P1, with the associated increase in the temperature, the material got softer allowing the plastic flow and the decrease of the compressive magnitude. The cooling stage led to a high tensile stress at the end on the analysis. These tensile stresses resulted from a contraction of this plastically deformed part restrained by an undeformed zone (far from the weld line).

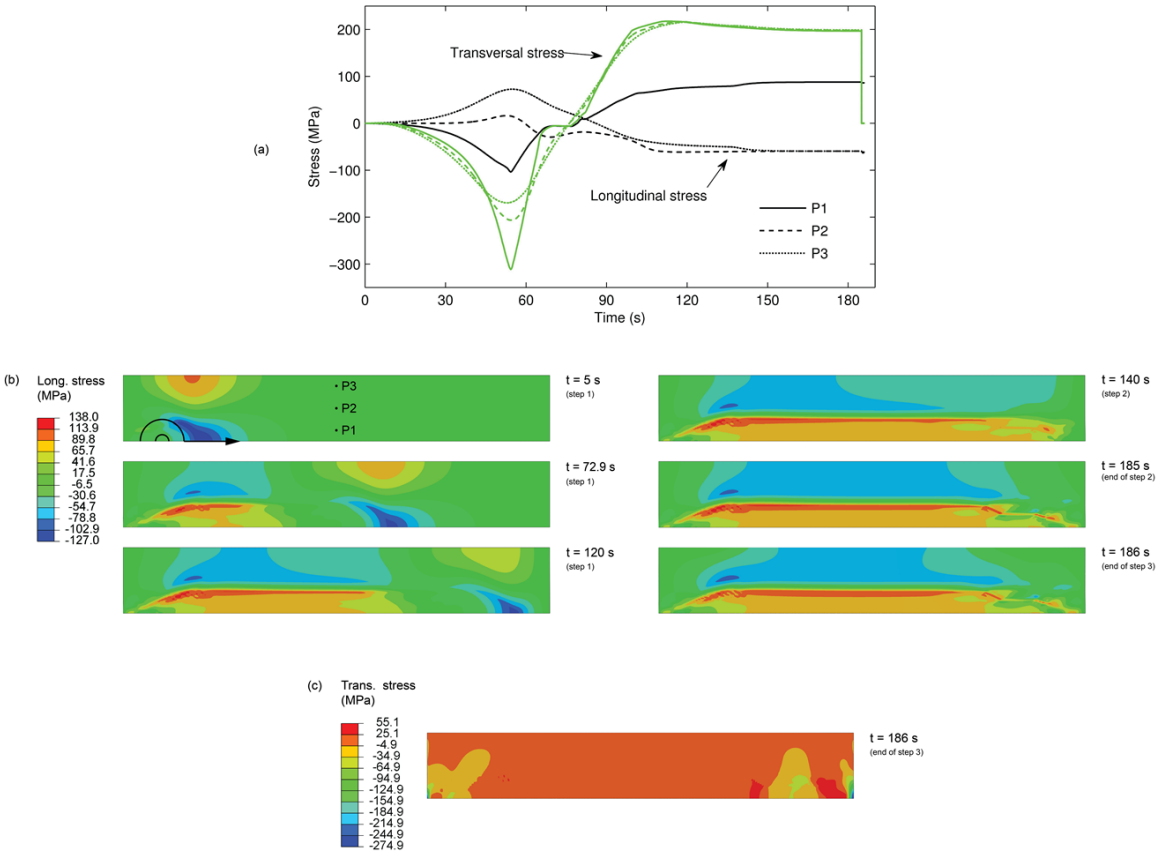

Figure 6: (a) Evolution stresses magnitude on three points located at the mid-length of the plate; (b) Longitudinal stresses during the FSW analysis; (c) Transverse stresses at the end of the analysis.

The longitudinal stress at points P2 and P3 equilibrated the stresses in P1, with mostly tensile stresses before the heat source passed by and a build-up of compressive stresses while cooling down. Since there are no restrictions in the longitudinal direction related to the clamping system, there is a small variation of the longitudinal stresses in step 3 of the simulation (when the plate support is removed) in all the three points. In terms of transverse component of stresses, the plots for all the points follow a similar pattern, with a higher absolute magnitude achieved closer to the weld line. In this case, high tensile stresses were built-up during the cooling, resulting from the previous plastic deformation in combination with the restrictions on the edge opposite to the weld line, along the *Ox* direction. Once these restrictions are removed (step 3), there is a high variation in the transverse stresses, leading to final values close to zero. Concerning the results at the end of the analysis - Figure 6 (c) - high compressive stress levels are seen close to the transverse edges of the plate, being the results in agreement to other published works [17],[30],[33].

Focusing on the *average* values across thickness, the longitudinal stress distribution at the end of the analysis is in good (qualitative) agreement with the experimental ones, as can be seen in Figure 7, where a map of the longitudinal stress of the entire mid-length section, as coming from the contour (experimental) method, is also represented.

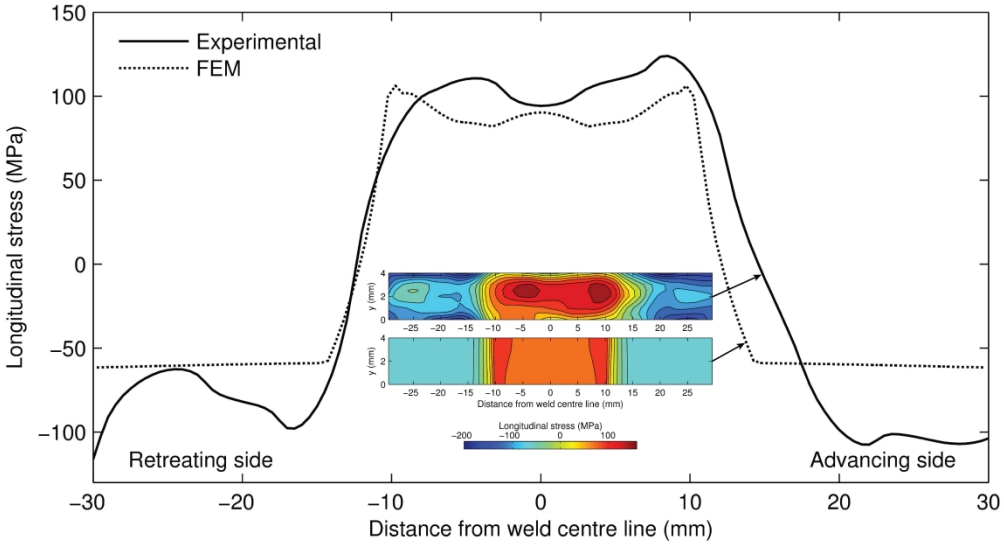

Figure 7: Longitudinal stress numerical results (average across thickness at the end of the simulation) from the FEM analysis and comparison with experimental results.

3.2 Industrial application: Modelling of stiffened panels obtained from FSW

3.2.1 Geometry of the stiffened panels

Simulations of the FSW process were performed on integrally stiffened panels having a single stiffener. Three different cross-section geometries were considered (Figure 8). The red lines represent the mid-thickness, used as reference for the modelling of the stiffened panels using shell finite elements, while the dimensions concern the size of those mid-thickness sections. The nomenclature for the panels geometries as mentioned in the figure is used in the description that follows. The panel with a T stiffener geometry (panel T) is based on the one presented at [41], and although this panel was originally designed for an aluminium alloy stronger than the AA2024-T3 (used in the present work), it has a 4 mm thick base plate, which is the same thickness of the plates previously validated in the FSW numerical model of the last sections. The other two geometries consist in variations of the previous one, now with a blade stiffener. The length of all the panels is the same (600 mm).

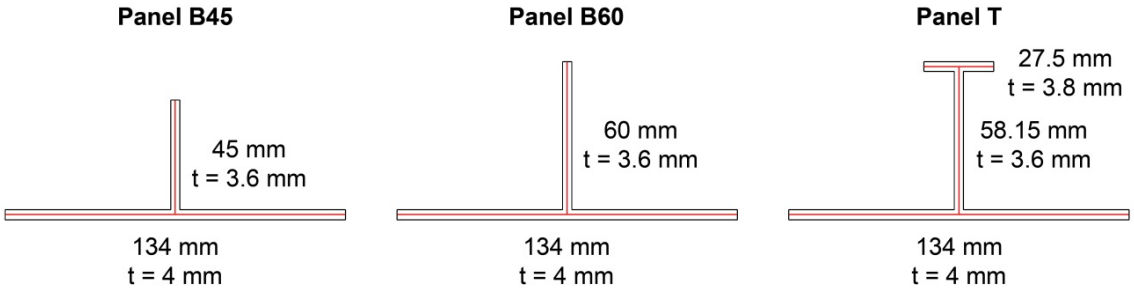

Figure 8: Cross-section of the stiffened panels with mid-thickness reference lines.

3.2.2 Boundary conditions

Following the previous discussions, FSW simulations included three steps as described in Table 2. In the first step, the heat source (corresponding to the tool) moved along the weld line and the linear velocity of the heat source was the same as used in the plate welding. Concerning the second step, the time step defined for the panel's cooling were enough to achieve temperatures not higher than 2º C above room temperature in the whole panel. The third step simulated the removal of the welding supports. After the welding analyses, a last step was included to add ageing effects, in which the material properties acquired the final yield stress magnitudes.

Table 2: CPU time effort involved in the FSW simulation of the stiffened panels.

Step	Action	CPU time effort (%)
1	Tool passage (heat input)	90.4%
2	Cooling	9.2%
3	Clamping system release	0.2%
Extra stage	Ageing	0.2%

Mechanical and thermal boundary conditions during each stage of the analysis are schematically represented in Figure 9 for panel T, being the same for the other geometries. In terms of the clamping system, a restriction was considered in the displacement along the *Oy* direction for all nodes located within 30 mm from the edge of the weld, reproducing a support needed to keep the base plate of the panel in contact with the support on the bottom. The boundary conditions on the edges opposite to the weld line aim to simulate a support to keep the weld edges of the panel together during the joining operation, and symmetry conditions were also imposed in the models.

Concerning the heat output, a heat transfer coefficient was set to 1000 $Wm^{-2}K$ at the bottom of the base plate of the panel, and in all remaining surfaces of the panel this variable was set to 20 $Wm^{-2}K$.

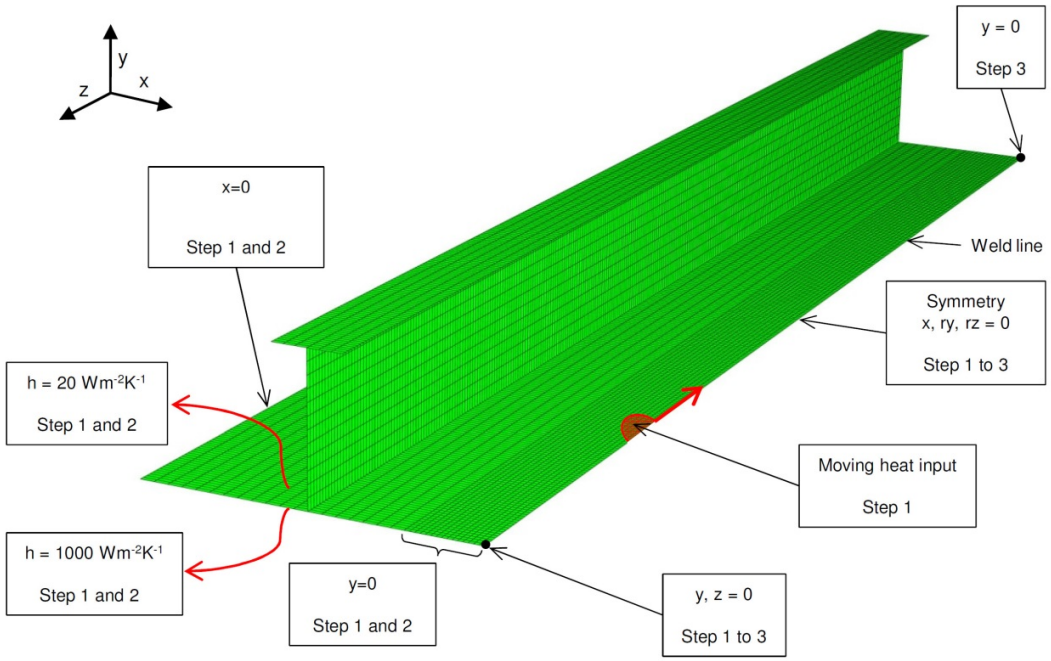

Figure 9: Thermal and mechanical boundary conditions for the simulation of the FSW process on the stiffened panels.

3.2.3 Sensitivity study on panel T

Sensitivity analyses were performed for the panel T model concerning different mesh refinement levels. One of the meshes used square elements with 2 mm side close to the weld line, while the other has square elements with 1 mm side in the same region. In the remaining area of the panels the elements are elongated in the transversal direction, since there is no need of a refined mesh far from the weld line.

In terms of number of elements, the first model has 15,600 elements while the second has 42,000 elements, leading to computational times of approximately 7 and 16 hours (using S4RT elements), respectively. Both meshes led to similar results with very small variations (maximum of 7 MPa) mainly due to spatial resolution factors (i.e. spatial location of integration points). It is thus assumed that the results obtained with the 2 mm mesh showed enough accuracy, being used in the remaining analyses. The preliminary sensitivity analyses showed that full integration elements (S4T) or the use of more than 5 integration points across thickness did not lead to significant differences in the results. Consequently, the combination of the S4RT formulation with 5 integration points across thickness was used in all the remaining simulations.

3.2.4 Softening distribution

In terms of material softening, the effects of the FSW on the panel T can be seen in Figure 10 (a) and (b), for the distribution: (i) along the entire panel, and (ii) on mid-length section, respectively. The results obtained for the panels with blade stiffeners (B45 and B60) were similar to those obtained for the panel T and, consequently, they are not represented. All results are presented in terms of the distribution of softening. Nevertheless, the distribution of the yield stress in the end of the welding simulation directly correlates to the one for the softening, considering minimum and maximum magnitudes of 205 and 345 MPa for softening values of 0.0 and 1.0, respectively, and according to equation (1).

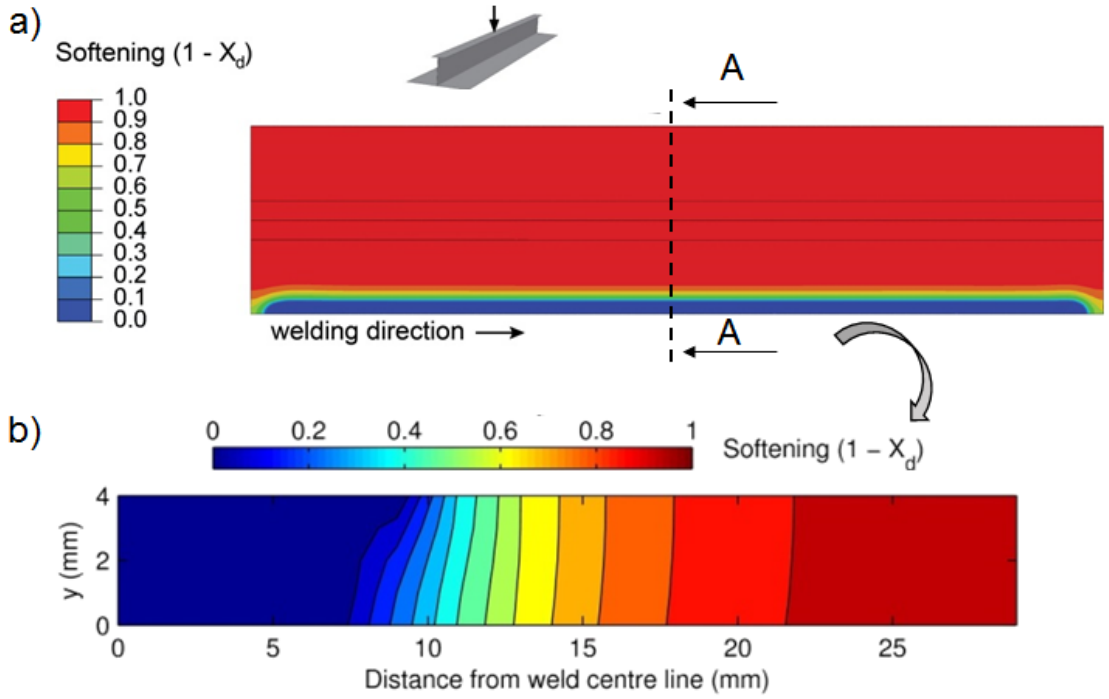

Figure 10: (a) Softening distribution on the panels T (top view); (b) Softening on the mid-length section A-A of the base plate of the panel T.

Comparing the stiffened panel results with those obtained for single plate, the zone with lower softening value (0.0) is narrower and the softening is higher in the interval (10, 30) mm, which is related to the lower temperatures achieved in this case. In a zone far from the weld line (for a distance higher than 30 mm) the material has properties very similar to the initial ones (base material), with a softening magnitude above 0.98. The variation of softening across thickness, as shown in Figure 10 (b), is more visible at the centre and higher than in the plate's case. Apart from that zone, however, the differences between the top and the bottom surfaces are very small (lower than 0.001 for locations further than 30 mm from the weld line). As for the single plate simulation, the ageing step consisted in raising the magnitude of the minimum yield stress (associated with the fully softened material) from 205 MPa (60% of the base material yield stress) to 259 MPa (75% of the base material yield stress). Results in Figure 11 show the yield stress profile along the mid-

thickness of the mid-length section, before and after the ageing effects were added to the model. As mentioned before, this procedure showed no influence neither on the residual stress distributions nor the nodal displacements.

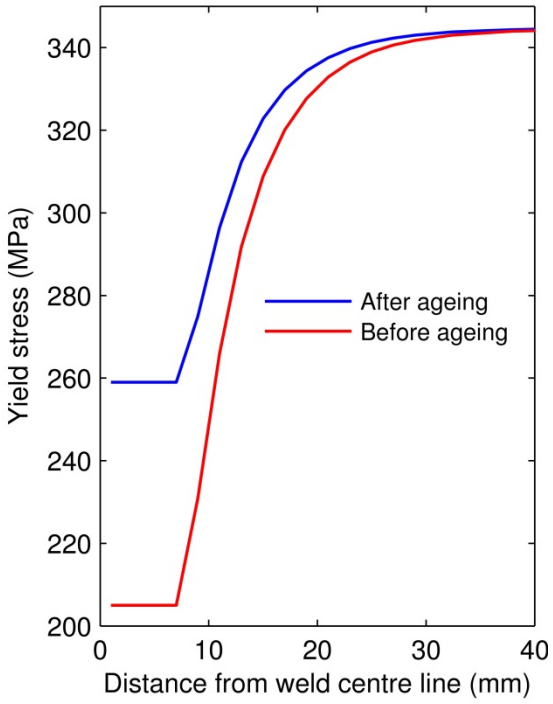

Figure 11: Yield stress profile along the mid-thickness of the mid-length section of the base plate of the panel T, before and after the ageing step.

3.2.5 Stress field

Longitudinal and transverse stress residual stress distributions for the panel T are shown in Figure 12. Significant difference between the panels with different cross-section geometry can be seen in Figure 13, consisting in variations of the longitudinal stress on the stiffeners, particularly at their mid-length. To better understand this difference, it should be noted that during cooling on the FSW process the arising of longitudinal tensile stresses close to the weld line is compensated by compressive stresses in the remaining part of the panel. This stress distribution forces the structure to bend, creating a convex shape in the longitudinal direction. The presence of the stiffeners minimises this effect, since they resist the distortion that, in turn, lead to a raise of the longitudinal

stresses in the stiffener. As expected, in the panel with a lower (cross-section) second moment of inertia about the *Ox* direction (panel B45) the longitudinal stresses in the stiffener are higher.

As previously mentioned, the typical M shape distribution was obtained for the longitudinal stresses along the mid-length of the panel. The maximum tensile magnitude is much higher (approximately 100 MPa) when compared with the single plate results. This comes from the fact that in the single plate models there were no restrictions along the longitudinal direction on the edge opposite to the weld line, while in the stiffened panel, at the same location (30 mm from the weld line), the remaining part of the base plate is an additional constraint for the displacement in longitudinal direction. This restriction leads to higher compressive stresses on the panels during the tool passage, which are responsible for higher plastic strain and higher tensile residual stresses after cooling.

On the contrary, the compressive stresses that exist farther from the weld line are much lower (in terms of absolute magnitudes) on the stiffened panels than in the single plate. This can be explained by taking into consideration that the equilibrium of the tensile stresses (close to the weld line) is ensured by a much larger cross-section area on the stiffened panels, leading to larger distribution of the compressive force and, thus, to lower compressive stresses.

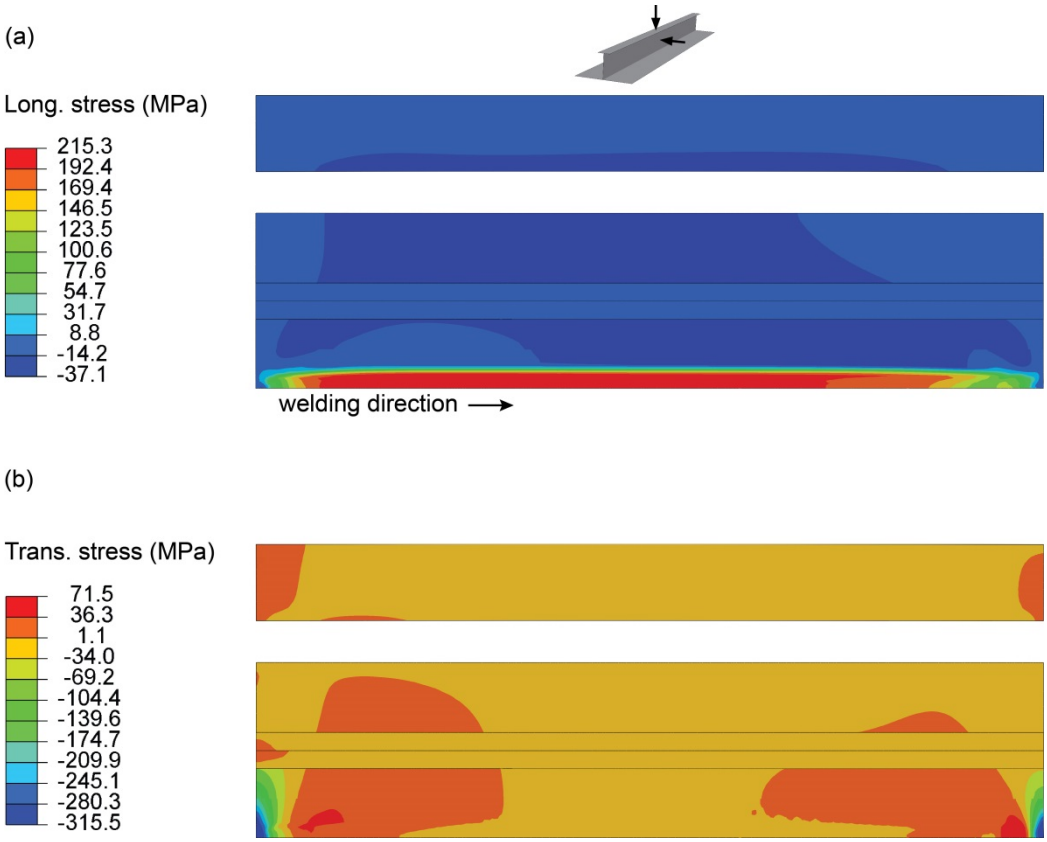

Figure 12: Stress distribution on the panels T: (a) longitudinal and (b) transverse stresses.

The distribution of the transverse residual stresses in Figure 12 (b) shows a high compressive stress close to both transverse edges of the panel, which equilibrates the small tensile stresses in the remaining area of the panels. In the mid-section the transversal stresses are close to zero, with maximum amplitude occurring on panel B45, with values between -1.72 and 0.01 MPa.

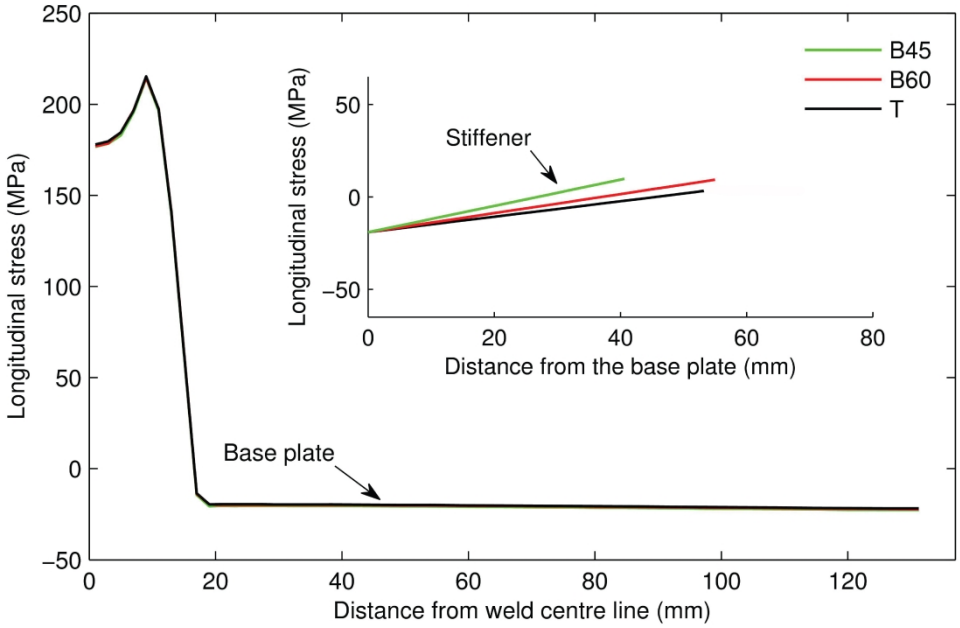

Figure 13: Longitudinal stresses on mid-length section of the panels (average across thickness).

The longitudinal stress distribution on the panel T mid-length section, presented in Figure 14, shows some degree of variation across thickness, that becomes more evident closer to the weld line, with the maximum variation (45 MPa) being achieved at 3 mm from the weld line. In the remaining parts of the panels, farther than 30 mm from the weld line (and not shown in Figure 14), the differences across thickness are smaller than 1 MPa. The results for panels B45 and B60 (also not shown) are similar to those of panel T in terms of stress magnitude and distribution.

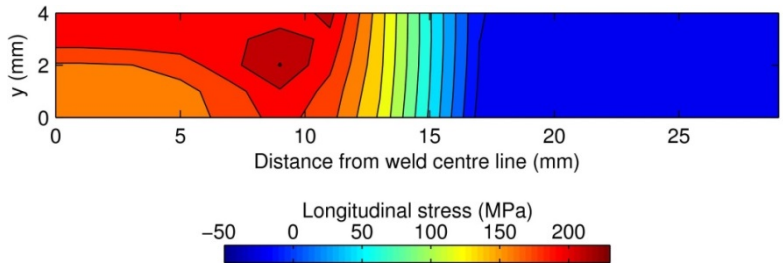

Figure 14: Longitudinal stresses distributions on mid-length section of the panel T (only the part closer to the weld line is shown).

3.2.6 Distortion effects

The deformed shape after welding can be seen in Figure 15 (a), while the out-of-plane displacements on the weld line and on the opposite edge are shown in Figure 15 (b). The typical distortion after FSW the process [42],[43], consisting of a hyperbolic parabolic shape, was correctly obtained. The V-shape in the transverse direction is quite similar for the whole set of tested panels in terms of displacement magnitude and nearly constant along the longitudinal direction in each panel. Concerning the longitudinal convex shape, the magnitude decreases for panels with higher (cross-section) second moment of inertia about the *Ox* direction (Figure 15 (b)), with stiffeners providing resistance to deformation coming from the residual stresses during the welding process. Therefore, panels with higher cross-section moment of inertia exhibit lower deformations together with lower longitudinal stresses in the stiffener.

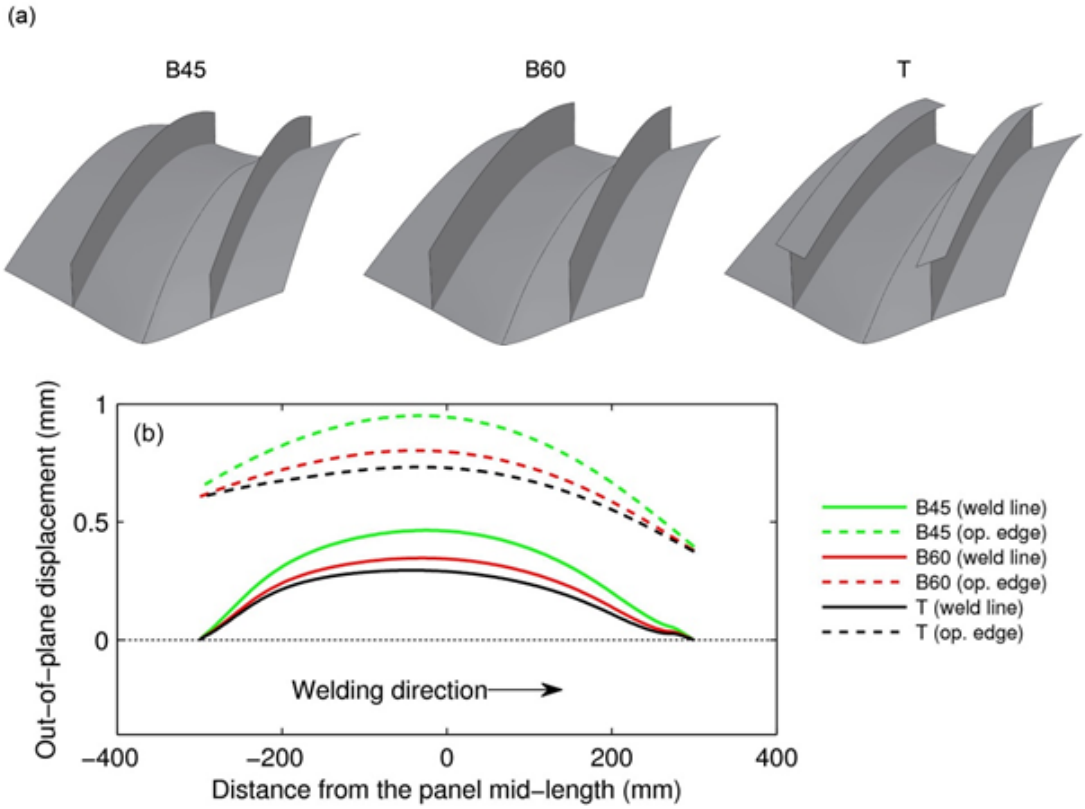

Figure 15: Distortion of the panels in the end of the FSW simulation: (a) Deformed shapes (symmetry plane on weld line; displacements amplified 50 times along *Oy*) and (b) Corresponding displacements at the end of the FSW simulation along the weld line and the opposite edge.

4. Conclusions

Considering the most distinctive features of the proposed model, the following conclusions and summary can be drawn:

- a shell-based finite element model was developed to simulate the transient thermal field and stress-strain distribution in a friction stir welding process;
- the numerical model was calibrated assuming a relatively simple benchmark, consisting of single plates joining by means of FSW process, used to validate residual stresses and mechanical properties variations by comparison with experimental data;
- the validated model was applied to simulate an industrial application dealing with the friction stir welding of integrally stiffened panels aiming to predict the welding effects in terms of residual stresses and distortions;
- three different single stiffener cross-section geometries were considered in the analyses: a panel with a T stiffener geometry (panel T) and other two panel geometries consist in a variation of the previous one, with blade stiffeners (panel B45 and panel B60);
- the residual stresses distribution results were quite similar for the different panels, except in the stiffeners zone;
- the distortion magnitude was also similar in terms of shape pattern but different in terms of magnitude, comparing results for panels with distinct cross-sections.

Following the achievements presented in this contribution, and using as a design tool the developed modelling and numerical simulation framework, the next steps of the authors will be the analysis and structural characterization of the behaviour of friction stir welded stiffened panels when

subjected to buckling loads. More specifically, influences of the joining processes on the compressive limit loads achieved by those panels will be investigated in subsequent works.

Acknowledgements

The authors wish to acknowledge the support given by *Fundação para a Ciência e a Tecnologia, Ministério para a Educação e Ciência*, Portugal, under the grants PTDC/EME-PME/113835/2009 and SFRH/BD/82456/2011.

References

[1] A. Alberg, M. Langseth, P.K. Larsen, Stiffened aluminium panels subjected to axial compression, Thin-Walled Structures 39 (2001) 861-885.

[2] R.S. Mishra, Z.Y. Maba, Friction stir welding and processing, Materials Science and Engineering 50 (2005) 1-78.

[3] G. Pouget, A.P. Reynolds, Residual stress and microstructure effects on fatigue crack growth in AA2050 friction stir welds, International Journal of Fatigue 30 (2008) 463–472.

[4] B.T. Gibson, D.H. Lammlein, T.J. Prater, W.R. Longhurst, C.D Cox, M.C. Ballun, K.J. Dharmaraj, G.E. Cook, A.M. Strauss, Friction stir welding: Process, automation, and control, Journal of Manufacturing Processes 16 (2014) 56–73.

[5] S. Zimmer, L. Langlois, J. Laye, R. Bigot, Experimental investigation of the influence of the FSW plunge processing parameters on the maximum generated force and torque, International Journal of Advanced Manufacturing Technology 47 (2010) 201-215.

[6] A. Murphy, W. McCune, D. Quinn, M. Price, The characterisation of friction stir welding process effects on stiffened panel buckling performance, Thin-Walled Structures 45 (2007) 339-351.

[7] A. Murphy, M. Price, R. Curran, Integration of strength and process modelling of friction-stir-welded fuselage panels, Journal of Aerospace Computing, Information and Communication 3 (2006) 159-176.

[8] G. Buffa, L. Fratini, G. Marannano, A. Pasta, Effect of the mutual position between weld seam and reinforcement on the residual stress distribution in Friction Stir Welding of AA6082 skin and stringer structures, Thin-Walled Structures 103 (2016) 62-71.

[9] ABAQUS, Abaqus Documentation (v.6.14). Simulia Dassault Systémes (2014).

[10] D. Quinn, A. Murphy, W. McEwan, F. Lemaitre, Stiffened panel stability behaviour and performance gains with plate prismatic sub-stiffening, Thin-Walled Structures 47 (2009) 1457-1468.

[11] C. Lynch, A. Murphy, M. Price, A. Gibson, The computational post buckling analyses of fuselage stiffened panels loaded in compression, Thin-Walled Structures 42 (2004) 1445-1464.

[12] J. Campbell, L. Hetey, R. Vignjevic, Non-linear idealisation error analysis of a metallic stiffened panel loaded in compression, Thin-Walled Structures 54 (2012) 44-53.

[13] J.F. Caseiro, R.A.F. Valente, A. Andrade-Campos, J.W. Yoon, Elasto-plastic buckling of integrally stiffened panels (ISP): An optimization approach for the design of cross-section profiles, Thin-Walled Structures 49 (2011) 864-873.

[14] J.F. Caseiro, R.A.F. Valente, A. Andrade-Campos, J.W. Yoon, On the elasto-plastic buckling of Integrally Stiffened Panels (ISP) joined by Friction Stir Welding (FSW): Numerical simulation and optimization algorithms, International Journal of Mechanical Sciences 76 (2013) 49-59.

[15] F. Al-Badour, N. Merah, A. Shuaib, A. Bazoune, Coupled Eulerian Lagrangian finite element modelling of friction stir welding processes, Journal of Materials Processing Technology 213 (2013) 1433-1439.

[16] W.A. Wall, M. Bischoff, K.U. Bletzinger, E. Ramm, Models and Finite Elements for Thin-walled Structures, in: Encyclopedia of Computational Mechanics, Volume 2: Solids, Structures and Coupled Problems, E. Stein, R. de Borst and T.J.R. Hughes (Eds.), John Wiley & Sons (2004) 1-25.

[17] M.R. Sonne, C.C. Tutum, J.H. Hattel, A. Simar, B. de Meester, The effect of hardening laws and thermal softening on modelling residual stresses in FSW of aluminium alloy 2024-T3, Journal of Materials Processing Technology 213 (2013) 477-486.

[18] C. Genevois, A. Deschamps, A. Denquin, B. Doisneau-cottignies, Quantitative investigation of precipiatation and mechanical behaviour for AA2024 friction stir welds. Acta Materialia 53 (2005) 2447-2458

[19] G. Buffa, A. Ducato, L. Fratini, Numerical procedure for residual stresses prediction in friction stir welding, Finite Elements in Analysis and Design Volume 47 (2011) 470-476

[20] A.M. Takhakh, H.N. Shakir, Experimental and numerical evaluation of friction stirs welding of AA2024-W aluminum alloy, Journal of Engineering 18 (2012) 717-734

[21] R.M.F. Paulo, P. Carlone, R.A.F. Valente, F. Teixeira-Dias, G.S. Palazzo, Numerical simulation of AA2024-T3 friction stir welding (FSW) process: Sensitivity analyses and influence of decisions during modelling stages, Key Engineering Materials 651-653 (2015) 919-924.

[22] P. Carlone, G.S. Palazzo, Influence of process parameters on microstructure and mechanical properties in AA2024-T3 friction stir welding, Metallogaphy Microstrucure and Analysis 2 (2013) 213-222.

[23] P. Carlone, G. Palazzo, Longitudinal Residual Stress Analysis in AA2024-T3 Friction Stir Welding, The Open Mechanical Engineering Journal 7 (2013) 18-26.

[24] M.B. Prime, Cross-sectional mapping of residual stresses by measuring the surface contour after a cut, Journal of Engineering Materials and Technology 123 (2001) 162-168.

[25] R.M.F. Paulo, P. Carlone, R.A.F. Valente, F. Teixeira-Dias, G.S. Palazzo, Influence of friction stir welding residual stresses on the compressive strength of aluminium alloy plates, Thin-Walled Structures 74 (2014) 184-190.

[26] Aerospace Specification Metals Inc., <asm.matweb.com> (March, 2012).

[27] R.V. Preston, H.R. Shercliff, P.J. Withers, S. Smith, Physically-based constitutive modelling of residual stress development in welding of aluminium alloy 2024, Acta Materialia 52 (2004) 4973-4983.

[28] R.M.F. Paulo, P. Carlone, R. Valente, F. Teixeira-Dias, G.S. Palazzo, Buckling analysis of aluminium alloy structures accounting for friction stir welding effect, Proceedings of the Ninth International Conference on Engineering Computational Technology, P. Iványi, B.H.V. Topping (Eds.), Naples, 2014.

[29] M.R. Sonne, P. Carlone, G.S. Palazzo, J.H. Hattel, Numerical modeling of AA2024-T3 friction stir welding process for residual stress evaluation, including softening effects, Key Engineering Materials 611-612 (2014) 1675-1682.

[30] D.G. Richards, P.B. Prangnell, S.W. Williams, P.J. Withers, Global mechanical tensioning for the management of residual stresses in welds, Materials Science and Engineering A 489 (2008) 351-362.

[31] D.G. Richards, P.B. Prangnell, P.J. Withers, S.W. Williams, T. Nagy, S. Morgan, Efficacy of active cooling for controlling residual stresses in friction stir welds, Science and Technology of Welding and Joining 15 (2010) 156-165.

[32] A. Bastier, M.H. Maitournam, F. Roger, K. Dang Van, Modelling of the residual state of friction stir welded plates, Journal of Materials Processing Technology 200 (2008) 25-37.

[33] Z. Feng, X.L. Wang, S.A. David, P.S. Sklad, Modelling of residual stresses and property distributions in friction stir welds of aluminium alloy 6061-T6, Science and Technology of Welding and Joining 12 (2007) 348-356.

[34] O.R. Myhr, Ø. Grong, Process modelling applied to 6082-T6 aluminium weldments - I. Reaction kinetics, Acta Metallurgica et Materialia 39 (1991) 2693-2702.

[35] R.W. McCune, A. Murphy, M. Price, J. Butterfield, The influence of friction stir welding idealization on residual stress and distortion predictions for future airframe assembly simulations, Journal of Manufacturing Science and Engineering 134 (2012).

[36] A.J. Leonard, Microstructure and ageing behaviour of FSWs in aluminium alloys 2014A-T651 and 7075-T651, Proceedings of the 2nd International Symposium on 'Friction Stir Welding', Gothenburg (2000).

[37] C.B. Fuller, M.W. Mahoney, M. Calabrese, L. Micona, Evolution of microstructure and mechanical properties in naturally aged 7050 and 7075 Al friction stir welds, Materials Science and Engineering: A 527 (2010) 2233-2240.

[38] A. Pastor, H.G. Svoboda, Time-evolution of Heat Affected Zone (HAZ) of Friction Stir Welds of AA7075-T651, Journal of Materials Physics and Chemistry 1 (2013) 58-64.

[39] M.Z.H. Khandkar, J.A. Khan, A.P. Reynolds, M.A. Sutton, Predicting residual thermal stresses in friction stir welded metals, Journal of Materials Processing Technology 174 (2006) 195-203.

[40] H. Schmidt, J. Hattel, A local model for the thermomechanical conditions in friction stir welding, Modelling and Simulation in Materials Science and Engineering 13 (2005) 77-93.

[41] J.W. Yoon, G.H. Bray, R.A.F. Valente, T.E.R. Childs, Buckling analysis for an integrally stiffened panel structure with a friction stir weld, Thin-Walled Structures 47 (2009) 1608-1622.

[42] D. Yan, A. Wu, J. Silvanus, Q. Shi, Predicting residual distortion of aluminium alloy stiffened sheet after friction stir welding by numerical simulation, Materials and Design 32 (2011) 2284-2291.

[43] Q.Y. Shi, J. Silvanus, Y. Liu, D.Y. Yan, H.K. Li, Experimental study on distortion of Al-6013 plate after friction stir welding, Science and Technology of Welding and Joining 13 (2008) 472-478.

Highlights (Thin Walled Structures international journal)

- A shell-based finite element model is proposed to model and numerically simulate friction stir welding (FSW) processes on aluminium plates.
- The numerical model relies on the validation of constitutive parameters against experimental data, namely residual stresses and hardness profiles.
- The model is further extended to predict residual stresses, geometric distortions, and softening distribution in friction stir welded stiffened panels.

Shell-based finite element model of single plates FSW process

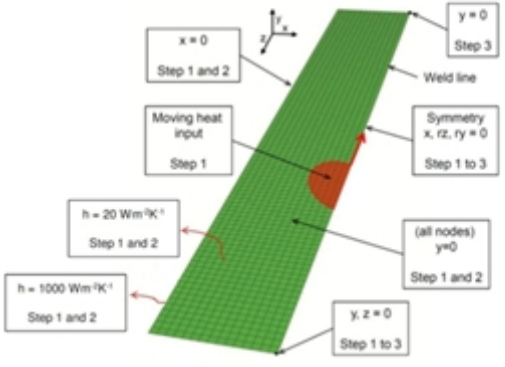

Numerical-Experimental validation

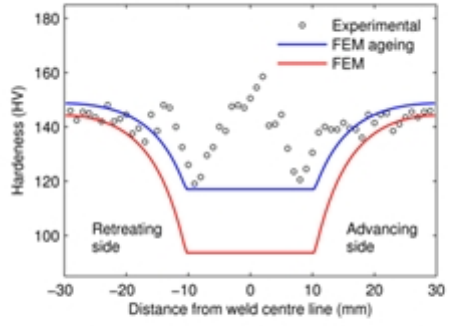

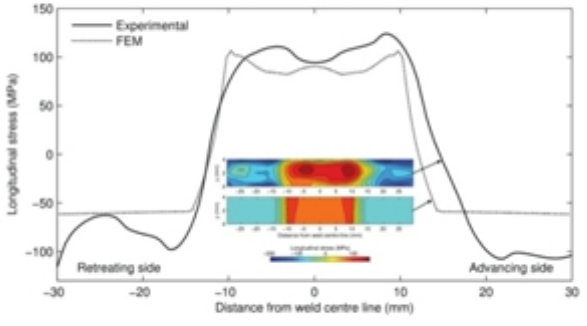

Shell-based finite element model of stiffened panel FSW process

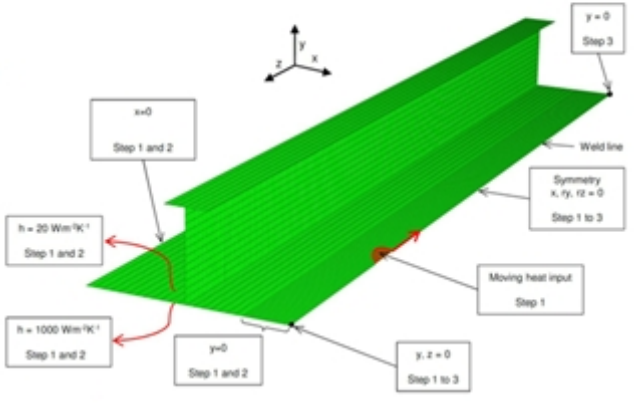

Prediction of residual stresses and distortions

Prediction of Friction Stir Welding effects on AA2024-T3 plates and stiffened panels using a shell-based finite element model

R.M.F. Paulo[1], P. Carlone[2], V. Paradiso[2], R.A.F. Valente[1,a], F. Teixeira-Dias[3],

[1]GRIDS Research Group, Department of Mechanical Engineering, University of Aveiro, Portugal

[2]Department of Industrial Engineering, University of Salerno, Italy

[3]Institute for Infrastructure and Environment, School of Engineering, The University of Edinburgh, United Kingdom

[a] *Corresponding author: robertt@ua.pt (Robertt Valente)*

Abstract (max. 100):

Manufacturing-induced effects significantly affect in-service behaviour of welded structures, such as integrally stiffened panels for aeronautic applications. Being a complex phenomenon with several variables involved, the assessment of the effects coming from welding usually relies on numerical simulations. Here, a novel shell-based finite element model is proposed to accurately simulate the transient thermal fields and stress-strain distributions resulting from friction stir welding (FSW) processes. The capability of the model to predict (i) residual stresses, (ii) material softening and (iii) geometric distortion of the welded parts is assessed by the modelling and simulation of FSW applied on aluminium integrally stiffened panels.

Keywords (max. 6):

AA2024-T3; Friction Stir Welding; Shell finite elements; Residual stresses; Distortion; Stiffened panels.

1. Introduction

Stiffened panels are the common choice for structural elements subjected to bending and, particularly buckling loads, in several demanding applications with high strength/weight ratio, such as the case of airplane wings and fuselages but also ships and off-shore structures. By means of a proper choice of the material as well as essential geometric parameters (particularly the cross sectional dimensions), these structures are supposed to withstand complex load scenarios. Indeed, complex solicitation pattern derive from the combination of longitudinal compressive (buckling) forces, transverse loads, in-plane shear forces, and those perpendicular to the base plate (inducing bending effects) [1]. For this reason, the modelling and prediction of geometric deviations are of crucial importance, particularly those coming from the joining operations of individual panels.

The application of friction stir welding (FSW) processes to join integrally stiffened panels has recently been investigated as an alternative of other joining techniques, such as riveting or fusion welding processes [2-4]. FSW is a well-established solid state welding process that enables to efficiently weld almost all types of aluminium alloys, even those traditionally classified as non-weldable by fusion welding means [5]. Although the effects coming from FSW processes, in terms of residual stresses and geometric distortion during and after joining, are proved to be less invasive compared to other joining processes, the impact of such effects on the performances of the welded structure should be carefully assessed [6-8].

In this study, modelling and numerical analyses of FSW processes were performed using the FEM commercial software package Abaqus [9]. One of the main characteristics of the proposed numerical finite element framework is that the parts to be welded were modelled exclusively using shell finite elements. Regarding the use of Abaqus package, many shell elements have been tested by several authors [10-12]. Nonetheless, some authors adopted solid elements in their models [13-15]. It is agreed that shell elements makes the meshing process simpler and faster, when compared to using solid elements, relying on a reference surface, usually in the mid-thickness of plate, where

the nodes are located. In terms of analysis, shell elements provide less computational time in contrast to solid ones, mainly due to the lower number of elements to be used in the model. Moreover shell elements allow for a more straightforward discretization of thin-walled structures, at the same time avoiding to a greater extent over-stiffness effects coming from transverse shear locking. Thin-walled structures like plates and shells are the most common construction elements in nature and technology [16]. Plate and shell structures are often reinforced with slender stiffeners, increasing the load-carrying capacity of thin-walled structures without giving up their lightweight property. To this purpose, a numerical modelling approach is of fundamental importance in the understanding of FSW process effects on the structural behaviour of stiffened panels in order to avoid conservative design choices, often motivated by an attempt to compensate for structural analysis uncertainties.

A 3-stage procedure was created, verified and adopted as a modelling and numerical framework that can be replicated by other researchers and industry partners, by means of a coupled thermo-mechanical model and a sequence of quasi-static analysis. The summary of the proposed modelling framework is covered in detail in the present paper. In the first stage, a heat source moved longitudinally along the welding line. On the second stage, a cooling step of the joined structure is promoted. During these two initial stages, mechanical boundary conditions were applied to simulate the clamping system. The third stage of the simulation corresponds to the release of the joined structure from the supports, where the boundary conditions are replaced by minimal constrains only to prevent rigid body movements. No remeshing procedures were needed to reduce the involved computational costs, which is an added value of the proposed modelling/simulation procedure. At the same time, temperature dependence of relevant material parameters was accounted for to ensure a reliable prediction and performance of the proposed numerical procedure. Additionally, thermal softening of the material was considered as being not only temperature dependent but also temperature history dependent, which is a distinctive feature of the presented approach.

The numerical models used in this study were firstly developed (and calibrated) in the simulation of a relatively simple benchmark consisting of single plates joining, being subsequently validated using reference experimental data, obtained by some of the present authors and commented in previous papers [17-19]. Doing so, AA2024-T3 plates were friction stir welded using a HSS unthreaded tool and subsequently microstructurally and mechanically characterized [18]. The residual stress levels coming from the joining process were inferred by the contour method [20], following the hybrid numerical–experimental procedure reported in [19]. The validated model was afterwards applied to simulate FSW process of stiffened panels for aeronautical applications.

2. Materials and Methods

The model of the welded plate, with the same dimensions of the one used in the experiments [21], was discretized using shell elements. A sensitivity study was carried out on the proper mesh density needed, the type of shell element to be chosen and the optimum number of integration point across thickness, seeking for a reasonable calculation time without compromising the accuracy of the results. Different types of heat source distribution were tested and the sensitivity of the numerical model to distinct mechanical boundary conditions (simulating the clamping system) was also assessed. Details concerning material modelling, element formulation, discretization, boundary and loading conditions are detailed presented in the following sections.

2.1 Material modeling

In the present work thermal and mechanical properties of AA2024-T3 were defined following previous references in the literature [18,22,23]. Thermal conductivity, thermal expansion coefficient, specific heat capacity, Young's modulus and yield stress were considered as being temperature dependent, whereas density and Poisson's ratio were assumed as temperature independent. An isotropic material model was applied for all the parameters. The material was considered to behave as perfectly plastic and therefore no hardening law was defined in the

constitutive model. In fact, Preston et al. [24] described an insignificant effect of work hardening, compared with the perfectly plastic case, on residual stresses numerically predicted for FSW processes with AA2024-T3, since most of the plastic strain occurs at high temperatures when work hardening rates are negligible. Additionally, the assumption of a perfectly plastic behaviour can lead to gains in terms of computational time, since there is no need for updates on the hardening variables.

Thermal softening effects induced by thermal cycles were also considered including a softening model to properly account for the effects of the temperature and temperature history on the yield stress. Among others, Sonne *et al.* [22] showed that the use of a softening model can lead to important changes in the prediction of residual stresses, compared to the solely use of temperature dependent material properties [22,25-30]. In this regard, a softening model based on the proposal by Myrh and Grong [31] and relying on the overall level of precipitates dissolution and coarsening, was assumed and implemented in the present work. Following the aforementioned contributions by Feng *et al.* [30] and Sonne *et al.* [22], the yield stress (σ) can be defined by:

$$\sigma = (\sigma_{\max} - \sigma_{\min})(1 - X_d) + \sigma_{\min}, \tag{1}$$

where $\sigma_{\max}$ is the yield stress of the material in the T3 condition, $\sigma_{\min}$ is the yield stress in the fully softened state and X_d is a dissolved precipitates fraction, defined by:

$$X_d = \sqrt{t_{eq}}. \tag{2}$$

In this equation, t_{eq} is given by:

$$t_{eq} = \sum_{i=1}^{N_{total}} \frac{\Delta t_i}{t_{ref} \exp\left[\frac{Q_{ref}}{R}\left(\frac{1}{T_i} - \frac{1}{T_{ref}}\right)\right]}, \tag{3}$$

where Δt_i is the size (time) of the increment, T_i is the current temperature, t_{ref} is the time for total dissolution at the reference temperature (T_{ref}) and defined according to Sonne *et al.* [22], R is the universal gas constant and Q_{ref} is the effective activation energy for the dissolution of precipitates.

Within a simulation run, for every increment the parameter X_{d} is updated at each integration point starting from a value of 0 (corresponding to the material in the T3 condition) and ranging up to 1 (a fully softened material), according to Eq. 2 and Eq. 3. The calculation of X_{d} was carried out by means of an Abaqus USDFLD user subroutine [9] developed by the authors, being this magnitude defined as a field variable. Actual values of yield stresses are then obtained by an interpolation between upper (σ_{max}) and lower (σ_{min}) bounds of the yield stress values, according to equation (1) and taking into account the current temperature. The curves corresponding to the upper and lower boundaries were based on the literature, although there are some differences in the information provided by different authors [22,24,27,32].

2.2 Model discretization

As previously mentioned, a shell element formulation was used to discretize the plates to be modelled. Two types of elements from the Abaqus library were tested: S4RT and S4T. These are 4-nodes thermo-mechanical coupled elements, where S4RT adopts a reduced integration scheme while S4T a fully integrated one [9]. Regarding the distribution of the integration points across thickness, a Simpson's rule is used by default in Abaqus [9]. Two different numbers of integration points were tested using the S4RT elements: 5 and 9 points across thickness. For the S4T shell element, only 5 integration points across thickness were used, resulting in a total of 20 integration points per element (5 layers of 4 in plane integration points). For this element, the option of 9 integration points across thickness was not tested since preliminary results using the S4RT element did not showed any advantages on using more than 5 integration points along the thickness direction. Three different mesh refinement levels with 0.5, 1, and 2 mm width were tested, all of

them composed by equal sized square elements. The reasoning behind the choice for regular meshes at this stage was related to infer if such a simple approach would be effective or, on the contrary, a local remeshing procedure would be needed. This study showed that the first option (the use of regular meshes) was enough for a good quality of results with a low effort in mesh generation and manipulation.

Furthermore, sensitivity analyses were performed concerning different mesh refinement levels, type of shell elements and number of integration point across thickness. Results of the sensitivity analyses showed that the use of full integration elements (S4T) instead of reduced integration (S4RT), or the use of more than 5 integration points across thickness, did not lead to significant differences in the results. Consequently, the combination of the S4RT formulation with 5 integration points across thickness, having a lower computational time, was used in all the remaining simulations. It was also inferred that a the most refined mesh (0.5 mm) led to a better resolution in mapping results, being this option therefore used in the subsequently analyses.

2.3 Loading and boundary conditions

The FSW numerical analyses included three different steps that are listed in Table 1, where it is also shown the relative duration (%) of each step, compared to the total CPU cost. Mechanical and thermal boundary conditions are allowed to vary from step to step during the simulation, closely following what happens with experimental conditions and as represented in Figure 1. After the welding analysis a last step was added to simulate the effects of ageing of the aluminium alloy, corresponding to an increase in the yield stress [33-35].

Table 1: FSW simulation steps, with the relative computational effort.

Step	Action	CPU time effort (%)
1	Tool passage (heat input)	72.2%

2	Cooling	26.8%
3	Clamping system release	0.5%
Extra stage	Ageing	0.5%

Concerning the mechanical boundary conditions, it is important to mention that the mechanical loads coming from the contact between the tool and the adjoining material were not considered in the numerical model, for the sake of simplicity. The inclusion of these loads can theoretically have influence on the residual stresses, namely leading to some degree of asymmetry between leading and retreating sides [32]. However, Richards *et al.* [27] concluded that these mechanical effects have a small overall impact when compared to the dominant thermal effects. It should be mentioned that this simplifying option is aligned to what is also adopted by other authors in the literature, with accurate results [22,26-28]. The current model presents a symmetry plane (in the weld line) in terms of geometry, loading conditions and boundary conditions, therefore only half of the assembly (one of the parts to be welded) was modelled, with obvious benefits in the total computational time. Thus, and as represented in Figure 1 (which depicts the FEM model of the friction stir butt welding of a couple of single plates), the nodes in the weld line were considered to have a symmetry boundary condition on the *Oyz* plane.

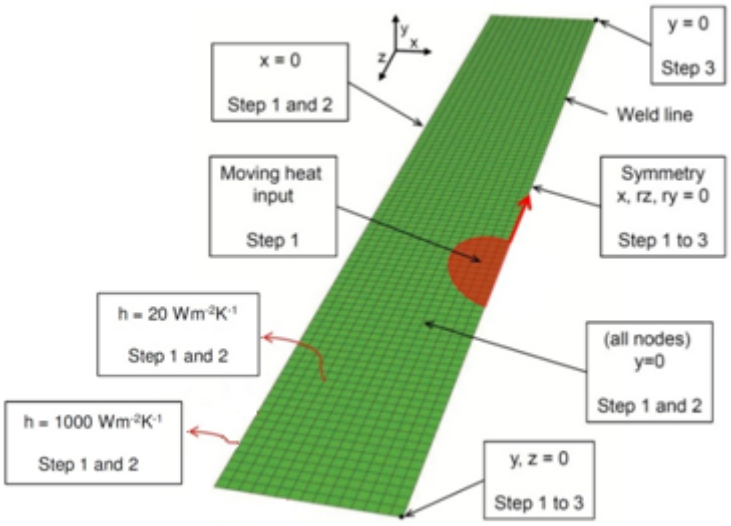

Figure 1: Boundary conditions (just half of the plate is shown, due to symmetry) [17].

Another concern was about the modelling of the clamping system. In this work, a simplifying approach was performed without physically defining the clamping tool, using only constrains in the displacement/rotations in some sets of nodes, as already adopted with good results in similar works in the literature [22,26,32]. In this case the modelling of contact surfaces, friction effects and clamping forces can be avoided. Using only displacement/rotation boundary conditions in the nodes, the best approach was found by trying several setups in preliminary analyses, as presented in a previous work [17].

The numerical results reported in [17] showed a high sensitivity of the numerical results to the mechanical boundary conditions used to model the clamping system. This can be related to the small width of the plate and consequent proximity of the displacement-restricted edge to the welded zone. The same sensitivity to boundary conditions was also inferred by Sonne *et al.* [26] in a study using plates with same width values. The set of boundary conditions represented in Figure 1 was chosen after preliminary analysis to reproduce the experimental clamping in the aforementioned case. In steps 1 and 2 (when the clamping system is present), displacements normal to the plate surface (along the *Oy* direction) were restricted, reproducing the effects of the base support and the

compression forces from the clamps. The displacement of nodes along the edge opposite to the weld line was also constrained in *Ox* direction (in the first two steps), reproducing the effects of the clamping system [21]. In step 3 of the simulation the boundary conditions related to the clamping are removed and a minimal set of constraints (necessary to avoid rigid body movements) is applied to the model. A similar strategy was applied also to simulate more complex structures, like the stiffened panels that are the subsequent goal of this study. In terms of thermal boundary conditions, the modelling of the heat transfer (in and out) during the first two steps of the simulation was performed according to information provided in the literature and taking into account the dimensions of the adopted tool. In step 3 of the numerical analyses, which occurs after the cooling of the plate, no heat transfer was considered.

During the first two steps, the heat flux output was modelled using distinct effective heat transfer coefficients for the top and for the bottom of the plate, following the equation:

$$q = -h(T - T^0), \quad (4)$$

where q is the heat flux across the surfaces, h is the heat transfer coefficient, T is the current temperature at the analysed point, and T^0 is the room temperature, which was set to 20º C. On the bottom surface of the plate, the heat transfer coefficient (h), related to the heat transfer between the plate and the steel base, was assumed to be 1000 $Wm^{-2}K^{-1}$, according to references in which similar analyses were performed [22,36,37]. At the top, the heat transfer coefficient (h) was set to 20 $Wm^{-2}K^{-1}$, accounting for convection heat transfer to the surrounding air [22,37] and also for some heat losses through the clamps. The time step for the cooling stage was determined after preliminary tests, which was found to be enough to induce temperatures lower that 1º C from room temperature in the whole plate. The total heat input provided the tool was also determined in preliminary analyses, by trial and error, approximating the numerical results in terms of the maximum temperature to the ones obtained experimentally [17]. A good agreement was found using a total power (Q) of 1300 W.

Paulo *et al.* [17] tested different heat input distributions using the same model. It was concluded that this parameter does not seem to have a significant influence on the stress and softening results if the mesh refinement is accounted for in the distributions, avoiding distinct total power inputs in different locations during the displacement of the heat source. Taking into account the conclusions remarked by Paulo *et al.* [17], a simple distribution [32], was used, resembling a pinless tool, where the heat input variation along the radius (r) follows the equation:

$$q(r) = \frac{3Qr}{2\pi(R_1^3 - R_0^3)}. \quad (4)$$

This equation was used for the heat input on the top surface of the plate, with R_0 and R_1 corresponding to the center (0) and shoulder limit (10 mm), respectively. The heat flux distribution was then implemented into the model by implementing an Abaqus DFLUX user subroutine [9], also responsible to define the position of the heat source advancing along the weld line. A preliminary convergence study was performed to define the mesh size as well as the maximum increment allowed during the tool travel, in order to achieve reasonable computational time and avoid artificial oscillations of temperature. The welding parameters were therefore defined according to the above mentioned procedure.

In the following section, a detailed description of the numerical results is presented for the single plates joining model, where a subsequent validation is conducted using reference experimental data following the hybrid numerical–experimental procedure. The validated model was afterwards applied to simulate the whole FSW process of stiffened panels, aiming to predict the welding effects on the structural behaviour.

3. Results and discussion

The implemented model was adopted to simulate two different cases. The former one represents a relatively simpler friction stir butt-welding process of two AA2024-T3 plates. This is performed for

calibration purposes, by comparison with experimental data, and also to highlight some mechanisms leading to material properties variations, as well as residual stresses development. In the latter case, and as mentioned before, an industrial application dealing with the friction stir welding of aeronautic stiffened panels is proposed.

3.1 Plate FSW process model

In this section, the simulation of the FSW process of two AA2024-T3 plates with 194 × 30 × 4 mm^3 is presented. The experimental trial is fully described in [21] and the simulation parameters were defined in accordance to this reference. In what follows, the data concerning the mapping of the full plate are relative to the top surface, where higher temperatures were achieved and the softening effect is more intense. It should also be mentioned, as a reference to a better understanding of the results, that the tool took 72.9 s to travel until the mid-length of the plate.

3.1.1 Softening and yield stress evolutions during FSW

The temperature evolution during the FSW process is responsible for variations on the softening value and the yield stress, represented in Figure 2 and Figure 3, respectively. From the results in Figure 2 it becomes evident that different temperature histories, being dependent on the distance from the welding line, can lead to distinct evolutions in the material softening. The minimum value of softening (0.0) can be found at the welding line, along most of the panel length after the welding. Along points that are at a distance more than 15 mm from the welding line, the values are in the meanwhile always higher than 0.45. Results given in Figure 3 give a clear idea that the yield stress magnitude is a result of combined effects of the temperature and of the temperature history (through the softening magnitude). In the end of the cooling stage, when the temperature of the plate is equal to the room temperature, a similar pattern in the distribution of the material softening and yield stress can be seen, since in this moment the yield stress is only dependent on the temperature history.

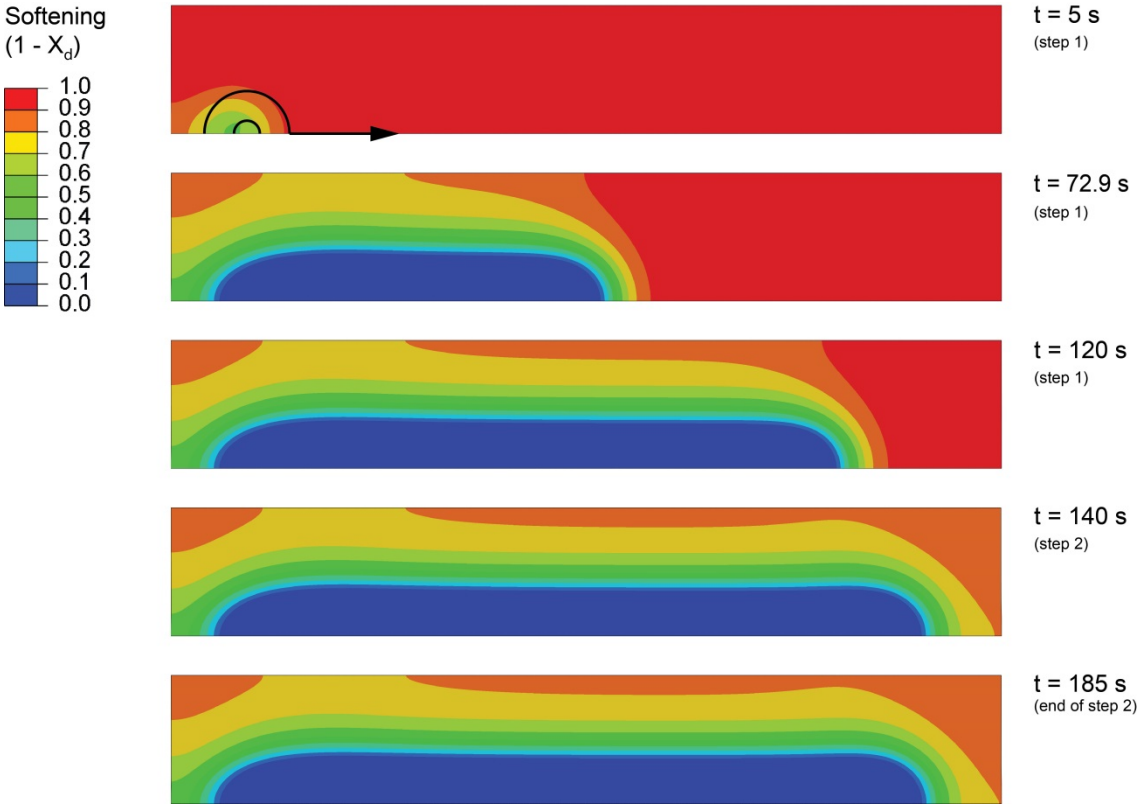

Figure 1: Evolution of material softening during the FSW analysis on the plate.

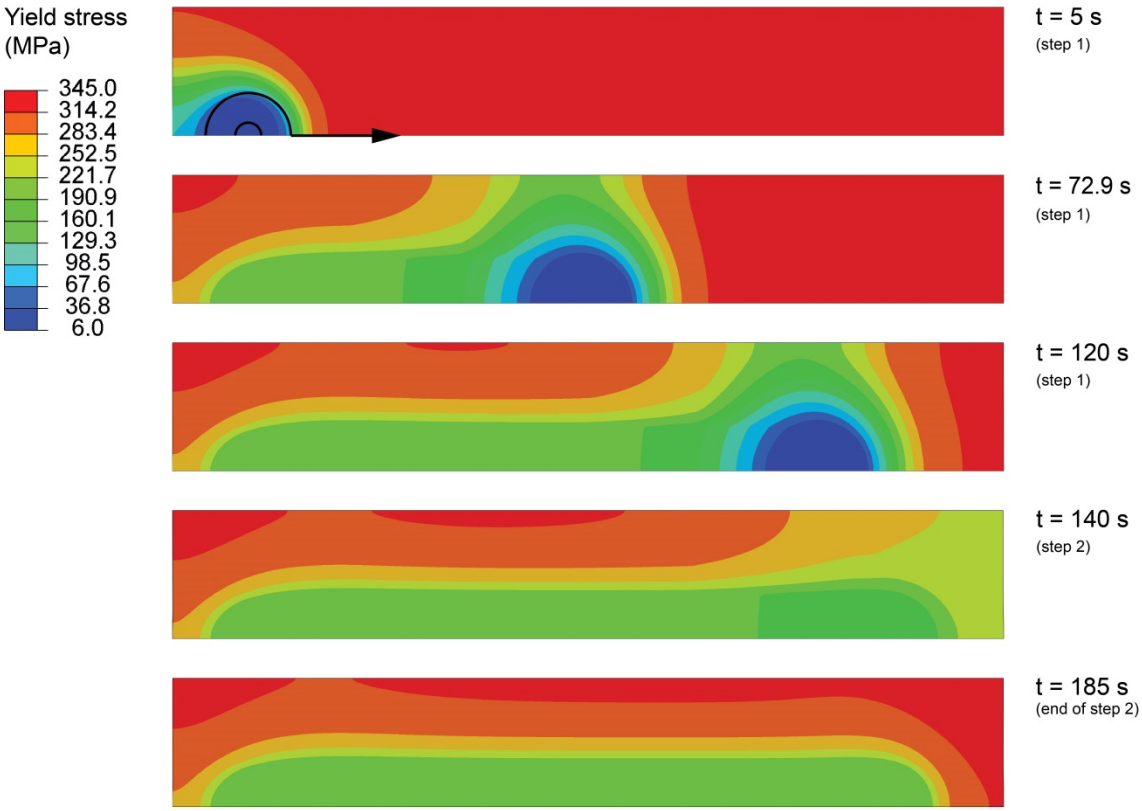

Figure 2: Yield stress evolution during the FSW analysis on the plate.

3.1.2 Ageing effects

It is well known that AA2024 is a precipitation-hardening alloy. Consequently, natural ageing occurs after a welding thermal cycle, and the re-precipitation process leads to a general improvement in mechanical properties, namely hardness and yield stress. To include the ageing effects in the hardness profile a simple methodology has been applied.

First of all, the hardness distribution established at the end of the welding process was inferred, assuming the same model used to calculate the yield stress (equation (1)) [22,30]. The hardness magnitude was therefore assumed to follow an equation of the type:

$$HV = (HV_{max} - HV_{min})(1 - X_d) + HV_{min}\ , \qquad (5)$$

where HV_{max} and HV_{min} were defined as 156 and 93 HV, respectively, considering the experimental outcomes discussed in [18]. Using equation (6), the hardness in the mid-thickness of the mid-length section, at the end of the FSW simulation, can be calculated using the softening values. The results are plotted in Figure 4 (solid red line) along with the experimental data. As can be seen, the experimentally measured hardness profile exhibits higher values, especially along the (-16, 16) mm interval, than those obtained from the numerical model. This occurrence was obviously attributed to some ageing effects. In this work, the mechanical properties recovery was simulated assuming a 40% increase of the X_d factor, established taking into account the experimental micro-hardness profile and then used to adjust also the yield stress distribution [18]. This second curve can be seen in Figure 4 (solid blue line).

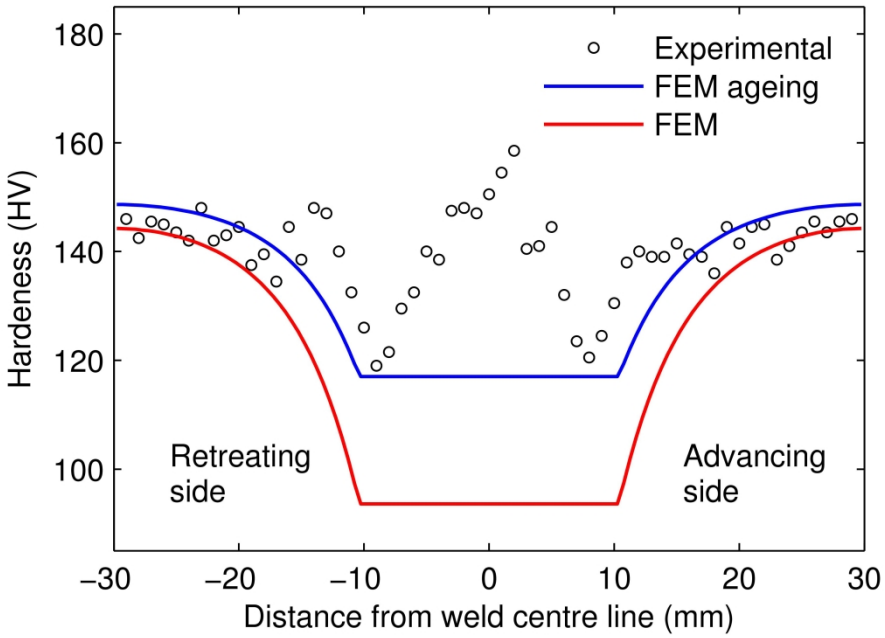

Figure 3: Comparison of the experimental hardness magnitude with the results obtained with the FEM model, before and after consideration of ageing effects [17].

The imposed ageing evolution follows what is usually verified in experimental measurements, consisting in a higher increase of the hardness in the zone more affected by the welding (close to the weld line) and a lower increase in the zone where the material is less affected by the welding [33]. Despite the aforementioned adjustments, it is worth noting the reliable prediction of the width of the HAZ, dictated by the micro-hardness variations. Obviously, this is not the case for the Nugget Zone (NZ) and Thermo-Mechanical Affected Zone (TMAZ) since the present models does not yet account for particular FSW effects that are dominant in these areas [17].

3.1.3 Longitudinal and transverse stress evolution during FSW

The distribution of longitudinal stresses during and after the FSW process, along with the distribution of transverse stresses at the end of the process itself, is shown in Figure 5. Since the changes in the yield stresses on ageing consist on an increase, they will not have any impact in the residual stress distribution or in the distorted shape. In the same Figure 5, variations can be seen

during welding of the longitudinal and transverse stresses in three points in the mid-length of the plate: P1, P2 and P3, that are located at 5, 15 and 25 mm from the weld line, respectively. It is agreed that magnitude of the longitudinal stress during the welding process had a distinct evolution depending on the distance to the weld line. A compressive peak occurred at point P1 before the heat source passed by, as a result of the thermal expansion in a position prior to this point. When the heat source got closer to P1, and with the associated increase in the temperature, the material got softer allowing plastic flow and the decrease of the compressive magnitude. Afterwards, with the cooling, occurred an increase of the magnitude of the stress, leading to a high tensile stress at the end on the analysis. These tensile stresses resulted from a contraction of this plastically deformed part restrained by an undeformed zone (far from the weld line).

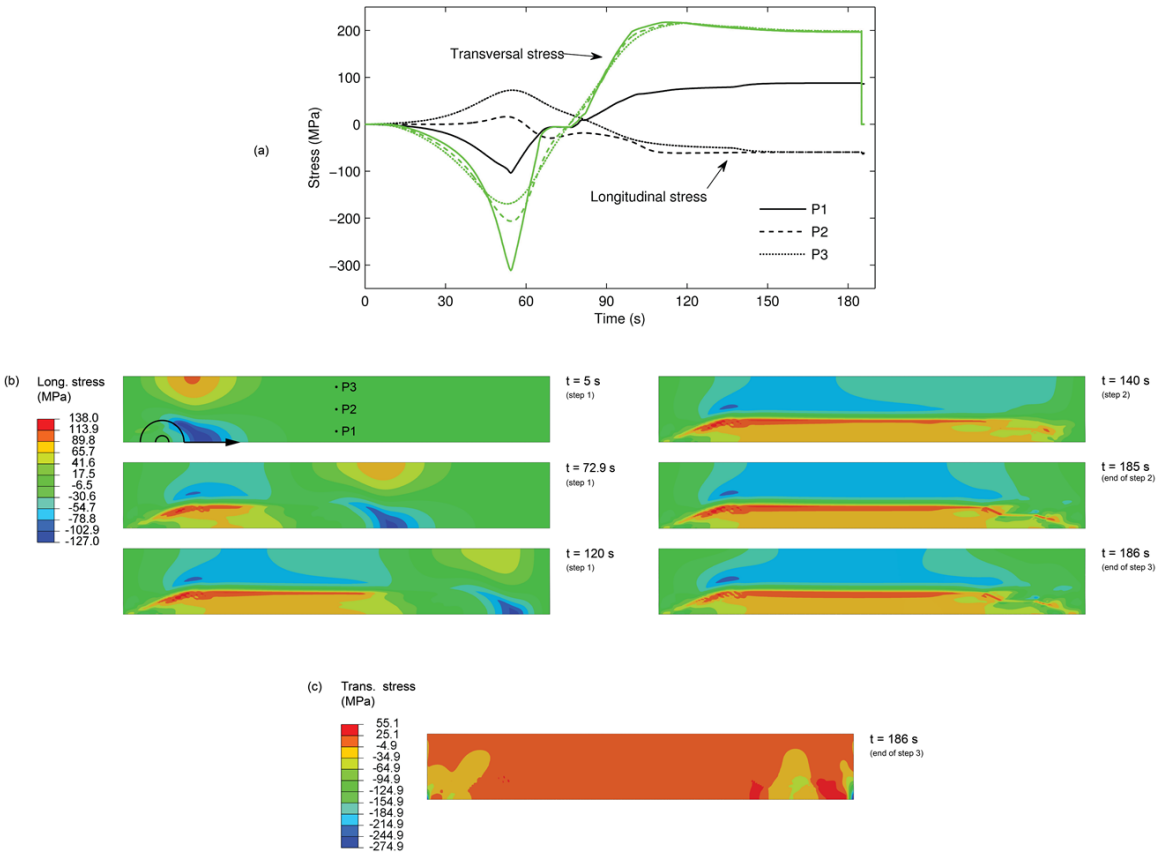

Figure 4: (a) Evolution stresses magnitude on three points located at the mid-length of the plate; (b) Longitudinal stresses during the FSW analysis; (c) Transverse stresses at the end of the analysis.

The longitudinal stress at points P2 and P3 equilibrated the stresses in P1, with mostly tensile stresses before the heat source passed by and a build-up of compressive stresses while cooling down. Since there are no restrictions in the longitudinal direction related to the clamping system, there is a small variation of the longitudinal stresses in step 3 of the simulation (when the plate support is removed) in all the three points. In terms of transverse component of stresses, the plots for all the points follow a similar pattern, with a higher absolute magnitude achieved closer to the weld line. In this case, high tensile stresses were built-up during the cooling, resulting from the previous plastic deformation in combination with the restrictions on the edge opposite to the weld line, along the *Ox* direction. Once these restrictions are removed (step 3), there is a high variation in the transverse stresses, leading to final values close to zero. Additionally, concerning the results at the end of the analysis, as shown in Figure 5 (c), it is possible to observe the existence of high compressive stress levels close to the transverse edges of the plate, which equilibrate the low tensile stresses in the remaining area of the plate. The results related to the evolution of stresses during welding are in agreement with the information provided in other works involving numerical simulation of the FSW process [22,27,30].

Concerning the validation of the model, and focusing on the average values across thickness, the longitudinal stress distribution obtained at the end of the analysis is in good agreement with the experimental results, as shown in Figure 6. Nevertheless, the results coming from the FEA show lower tensile peaks (approximately of 17 MPa). In the zone far from the weld centre line, with compressive stresses, the absolute magnitude is higher in the experimental curve since they equilibrate the higher tensile stresses at the centre. Although the validation using average across thickness is reliable, results in the sub-figure of Figure 6 show a map of the longitudinal stress of the entire mid-length section.

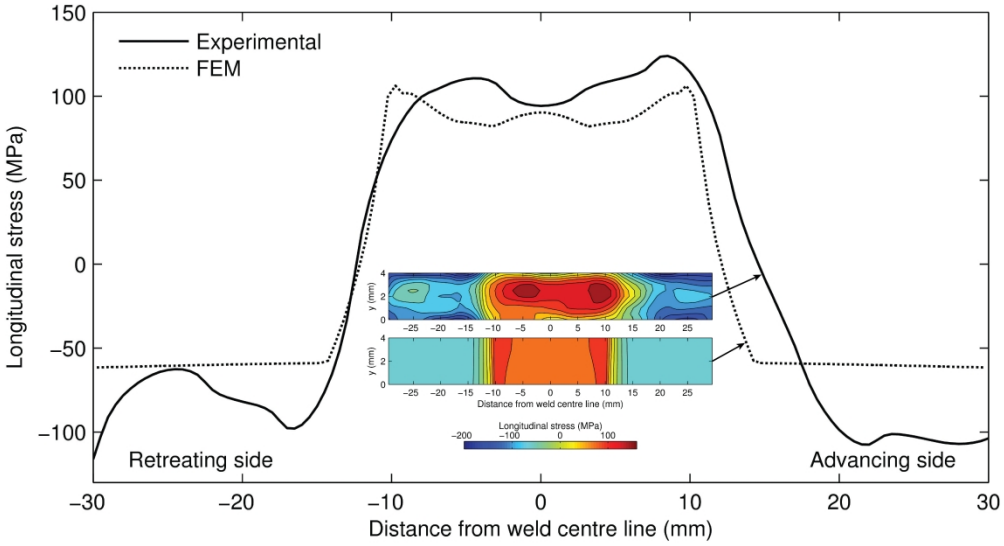

Figure 6: Longitudinal stress numerical results (average across thickness at the end of the simulation) from the FEM analysis and comparison with experimental results.

As a result, the proposed numerical model is also able to predict the longitudinal residual stresses with acceptable accuracy. After the described assessment and validation steps, the developed model was subsequently applied to simulate FSW process of stiffened panels, as described in the next section.

3.2 Industrial application: Modelling of stiffened panels obtained from FSW

The above described methodology for single plates welding was adapted and used to perform the simulation of an FSW process on stiffened panels, aiming to predict the resulting welding effects, as detailed in the following.

3.2.1 Geometry of the stiffened panels

Simulations of the FSW process were performed on integrally stiffened panels having a single stiffener. Three different cross-section geometries, as represented in Figure 7, were considered in

the analyses. The red lines represent the mid-thickness, used as reference for the modelling of the stiffened panels using shell finite elements, while the dimensions concern the size of those mid-thickness sections. Also, the nomenclature for the panels geometries as mentioned in the figure is used in the description that follows. The panel with a T stiffener geometry (panel T) is based on the one presented by Yoon *et al.* [38]. Although this panel was originally designed for an aluminium alloy stronger than the AA2024-T3 (used in the present work), it has a 4 mm thick base plate, which is the same thickness of the plates previously validated in the FSW numerical model of the last sections. The other two panel geometries consist in variations of the previous one, with a blade stiffener. The length of all the panels is the same, being equal to 600 mm.

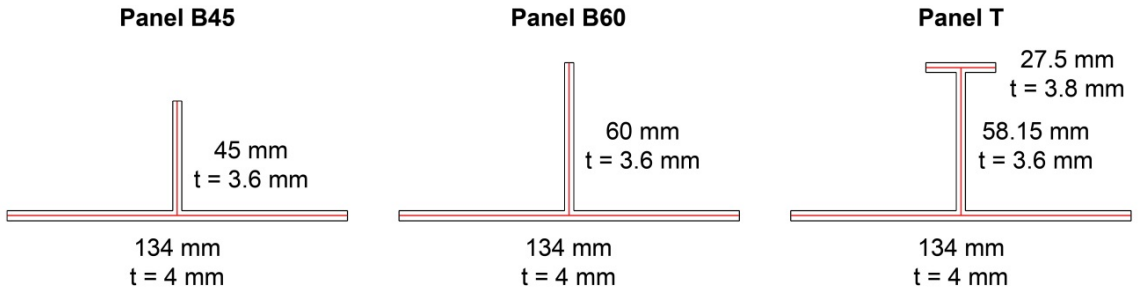

Figure 7: Cross-section of the stiffened panels with mid-thickness reference lines.

3.2.2 Boundary conditions

Following the procedure adopted for the single plate welding, the FSW simulation included three steps as described in Table 2. In the first step, the heat source (corresponding to the tool) moved along the weld line. The linear velocity of the heat source was the same used in the plate welding. Concerning the second step, the time step defined for the panel's cooling were enough to achieve temperatures not higher than 2º C above room temperature in the whole panel. The third step simulated the removal of the welding supports. Also following the procedures described before,

after the welding analyses a last step was included to add ageing effects, in which the material properties acquired the final yield stress magnitudes.

Table 2: CPU time effort involved in the FSW simulation of the stiffened panels.

Step	Action	CPU time effort (%)
1	Tool passage (heat input)	90.4%
2	Cooling	9.2%
3	Clamping system release	0.2%
Extra stage	Ageing	0.2%

The mechanical and thermal boundary conditions during each stage of the analysis are schematically represented in Figure 8, for the panel T, being the same for the remaining panel geometries. As with the previous models adopted for the plate welding, a symmetry boundary condition corresponding to the weld line was considered. In terms of the clamping system, a restriction was considered in the displacement along the *Oy* direction for all nodes located within 30 mm from the edge of the weld, reproducing a support needed to keep the base plate of the panel in contact with the support on the bottom. The boundary conditions on the edges opposite to the weld line aim to simulate a support to keep the weld edges of the panel together during the joining operation.

Concerning the heat output, a heat transfer coefficient was set to 1000 $Wm^{-2}K$ at the bottom of the base plate of the panel. In all remaining surfaces of the panel this variable was set to 20 $Wm^{-2}K$. In terms of heat input distribution, the different setups were tested in preliminary analyses using the panel T.

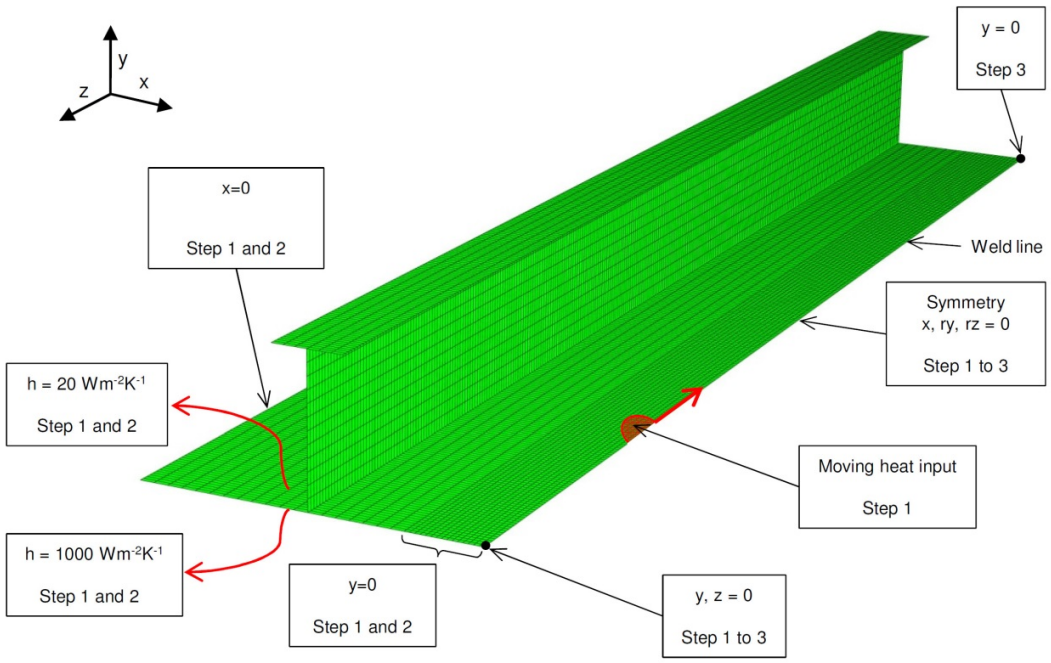

Figure 8: Thermal and mechanical boundary conditions for the simulation of the FSW process on the stiffened panels.

3.2.3 Sensitivity study on panel T

Considering that the results of the FSW simulation were somehow affected by the size of the plate, sensitivity analyses were also performed for the panel T model, concerning different mesh refinement levels. One of the meshes used square elements with 2 mm side close to the weld line, while the other has square elements with 1 mm side in the same region. In the remaining area of the panels the elements are elongated in the transversal direction, since there is no need of a refined mesh far from the weld line.

In terms of number of elements, the first model has 15,600 elements while the second has 42,000 elements, leading to computational times of approximately 7 and 16 hours (using S4RT elements), respectively. Both meshes tested led to similar results, with very small variations (maximum of 7 MPa) mainly due to spatial resolution factors (i.e. spatial location of the integration points). It is thus assumed that the results obtained with the 2 mm mesh showed enough accuracy, being used in

the remaining analyses. Additionally, the preliminary sensitivity analyses showed that the use of full integration elements (S4T) instead of reduced integration (S4RT), or the use of more than 5 integration points across thickness, did not lead to significant differences in the results. Consequently, the combination of the S4RT formulation with 5 integration points across thickness was used in all the remaining simulations, as this represented an increased computational performance with reliable results. As for the plate model, the heat input distribution also add an insignificant effect in the mesh refinement was taking into account in the distribution setting.

3.2.4 Softening distribution

In terms of material softening, the effects of the FSW on the panel T can be seen in Figure 9 (a) and (b), for the distribution: (i) along the entire panel, and (ii) on mid-length section, respectively. The results obtained for the panels with blade stiffeners (B45 and B60) were very similar to the ones obtained for the panel T and, consequently, they are not represented. All the results are presented in terms of the distribution of softening. Nevertheless, the distribution of the yield stress in the end of the welding simulation directly correlates to the one for the softening, considering minimum and maximum magnitudes of 205 and 345 MPa for softening values of 0.0 and 1.0, respectively, and according to equation (1).

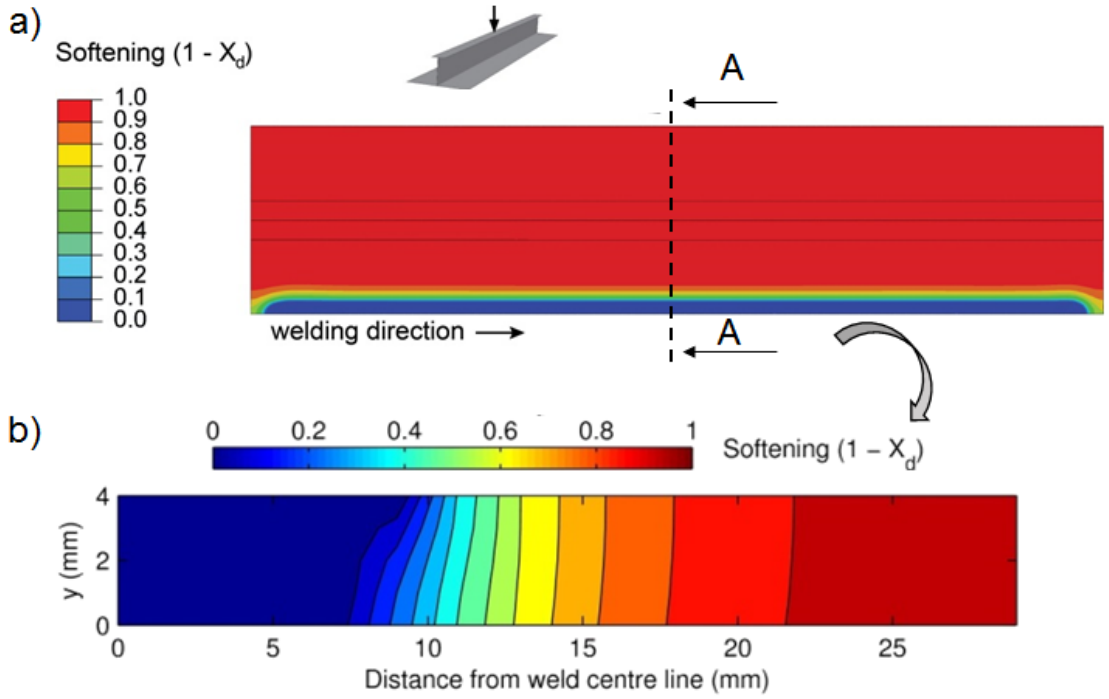

Figure 9: (a) Softening distribution on the panels T (top view); (b) Softening on the mid-length section A-A of the base plate of the panel T.

Comparing the stiffened panel results with those obtained for single plate, it can be seen that the zone with lower softening value (0.0) is narrower and the softening is higher in the interval (10, 30) mm. This is related to the lower temperatures achieved in the welding simulations of the stiffened panel compared to the simulations of the plate. The power of the heat input in the FSW analyses for both structures (stiffened panel and single plate) was the same. However, the stiffened panel has a much larger surface, leading to a higher heat loss, and larger volume, leading to higher heat conduction away from the location of the tool, reasons that together can explain the lower maximum temperature. In a zone far from the weld line (for a distance higher than 30 mm) the material has properties very similar to the initial ones (base material), with a softening magnitude above 0.98. The variation of the softening across thickness, as shown in Figure 9 (b), is more accentuated at the centre and higher than in the plate's case. Apart from that zone, however, the

differences between the top and the bottom surfaces are very small (lower than 0.001 for locations further than 30 mm from the weld line). As for the single plate simulation, the ageing step consisted in raising the magnitude of the minimum yield stress (associated with the fully softened material) from 205 MPa (60% of the base material yield stress) to 259 MPa (75% of the base material yield stress). Results in Figure 10 show the yield stress profile along the mid-thickness of the mid-length section, before and after the ageing effects were added to the model. As mentioned before, this procedure showed no influence neither on the residual stress distributions nor the nodal displacements.

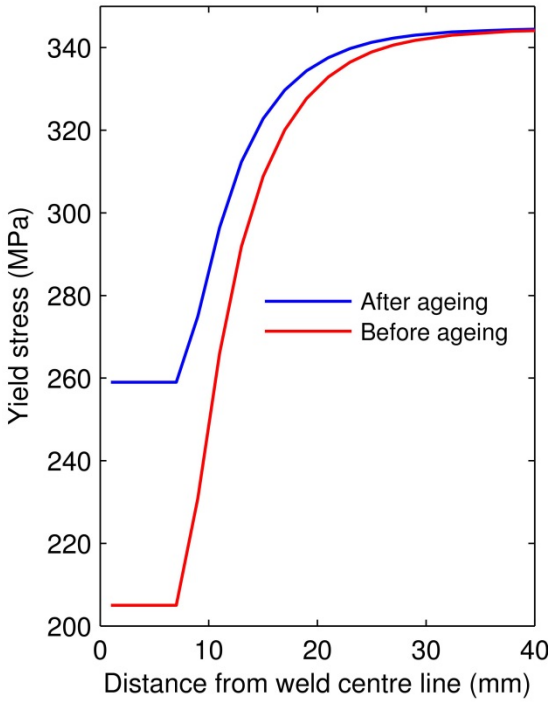

Figure 10: Yield stress profile along the mid-thickness of the mid-length section of the base plate of the panel T, before and after the ageing step.

3.2.5 Stress field

Longitudinal and transverse stress residual stress distributions for the panel T are shown in Figure 11. The only significant difference between the panels with different cross-section geometry can be

seen in Figure 12 and consists in variation of the longitudinal stress on the stiffeners, in particular at mid-length. To better understand this difference it should be noted that, during the cooling on the FSW process, the arising of longitudinal tensile stresses close to the weld line is compensated by compressive stresses in the remaining part of the panel. This stress distribution forces the structure to bend, creating a convex shape in the longitudinal direction. The presence of the stiffeners minimises this effect, since they offer resistance to the distortion that, in turn, lead to a raise of the longitudinal stresses in the stiffener. As expected, in the panel with a lower (cross-section) second moment of inertia about the *Ox* direction (panel B45) the longitudinal stresses in the stiffener are higher.

As previously mentioned, the typical M shape distribution was obtained for the longitudinal stresses along the mid-length of the panel. The maximum tensile magnitude is much higher (approximately 100 MPa) when compared with the single plate results. This is due to the fact that in the single plate models there were no restrictions along the longitudinal direction on the edge opposite to the weld line, while in the stiffened panel, at the same location (30 mm from the weld line), the remaining part of the base plate is an additional constraint for the displacement in longitudinal direction. This restriction leads to higher compressive stresses on the panels during the tool passage, which are responsible for higher plastic strain and higher tensile residual stresses after cooling.

On the contrary, the compressive stresses that exist farther from the weld line are much lower (in terms of absolute magnitudes) on the stiffened panels than in the single plate. This can be explained by taking into consideration that the equilibrium of the tensile stresses (close to the weld line) is ensured by a much larger cross-section area on the stiffened panels, leading to larger distribution of the compressive force and, thus, to lower compressive stresses.

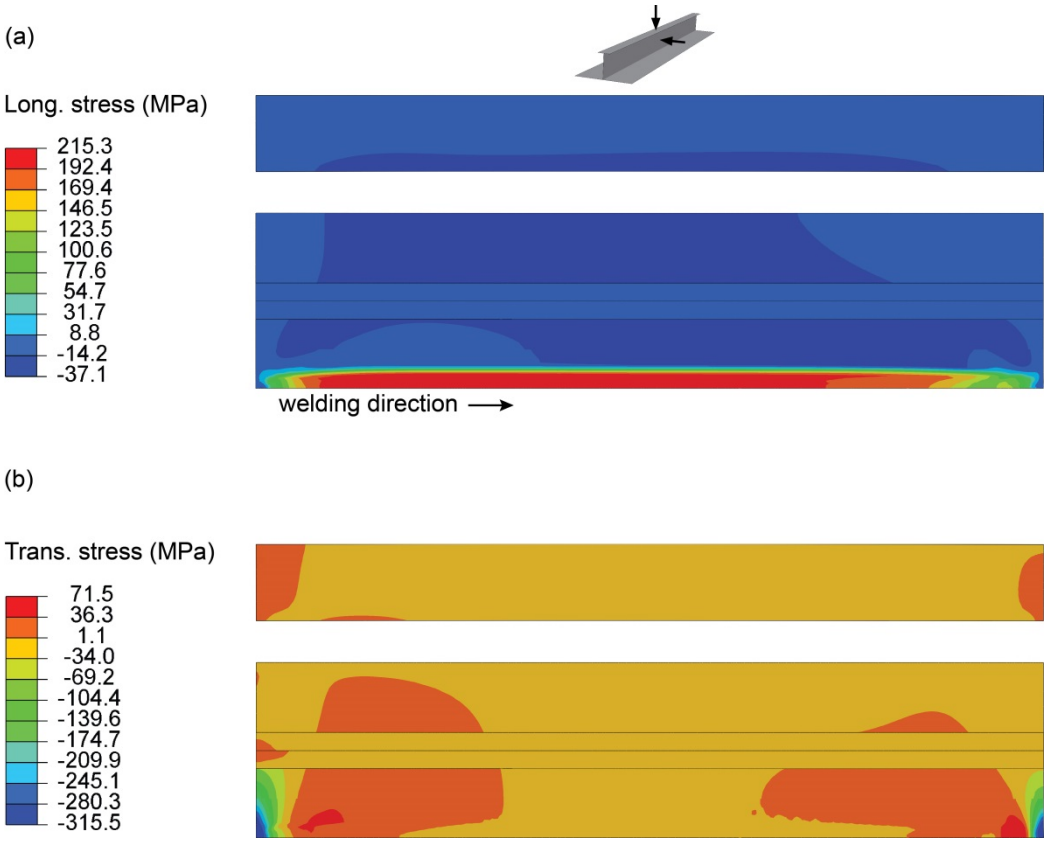

Figure 11: Stress distribution on the panels T: (a) longitudinal and (b) transverse stresses.

The distribution of the transverse residual stresses in Figure 11 (b) shows a high compressive stress close to both transverse edges of the panel, which equilibrates the small tensile stresses in the remaining area of the panels. In the panel mid-section the transversal stresses are close to zero, with maximum amplitude occurring on panel B45, with values between -1.72 and 0.01 MPa.

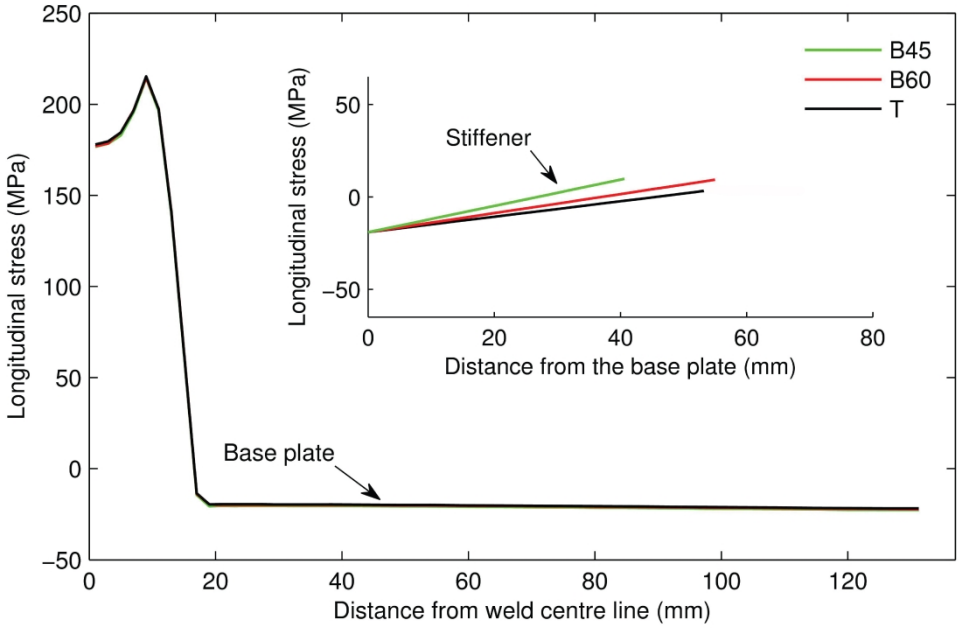

Figure 12: Longitudinal stresses on mid-length section of the panels (average across thickness).

The longitudinal stress distribution on the panel T mid-length section, presented in Figure 13, shows some degree of variation across thickness, that becomes more evident closer to the weld line, with the maximum variation (45 MPa) being achieved at 3 mm from the weld line. In the remaining parts of the panels, farther than 30 mm from the weld line (and not shown in Figure 13), the differences across thickness are smaller than 1 MPa. The results for panels B45 and B60 (also not shown) are very similar to ones for the panel T, in terms of stress magnitude and distribution.

It is also interesting to realise that the variations across thickness are much higher than what was obtained for the single plate welding. This can be explained by the lower influence of the mechanical boundary conditions that reproduce the clamping system in the stiffened panel model.

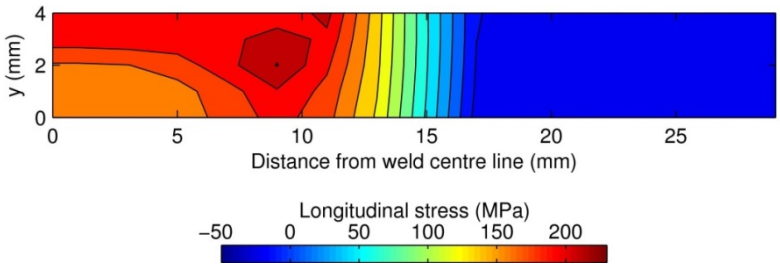

Figure 13: Longitudinal stresses distributions on mid-length section of the panel T (only the part closer to the weld line is shown).

3.2.6 Distortion

The deformed shape of the panels after welding can be seen in Figure 14 (a), while the out-of-plane displacements, on the weld line and on the opposite edge, are shown in Figure 14 (b). The typical distortion after FSW the process [39,40], consisting of a hyperbolic parabolic shape, was correctly obtained. The V-shape in the transverse direction is quite similar for the whole set of tested panels, in terms of displacement magnitude, and nearly constant along the longitudinal direction in each panel. Concerning the longitudinal convex shape, the magnitude decreases for panels with higher (cross-section) second moment of inertia about the *Ox* direction, as can be seen in Figure 14 (b). As previously mentioned, the stiffeners offer resistance to deformation forced by the residual stresses that arises during the welding process. Therefore, panels with higher cross-section moment of inertia exhibit lower deformation, together with lower longitudinal stresses in the stiffener.

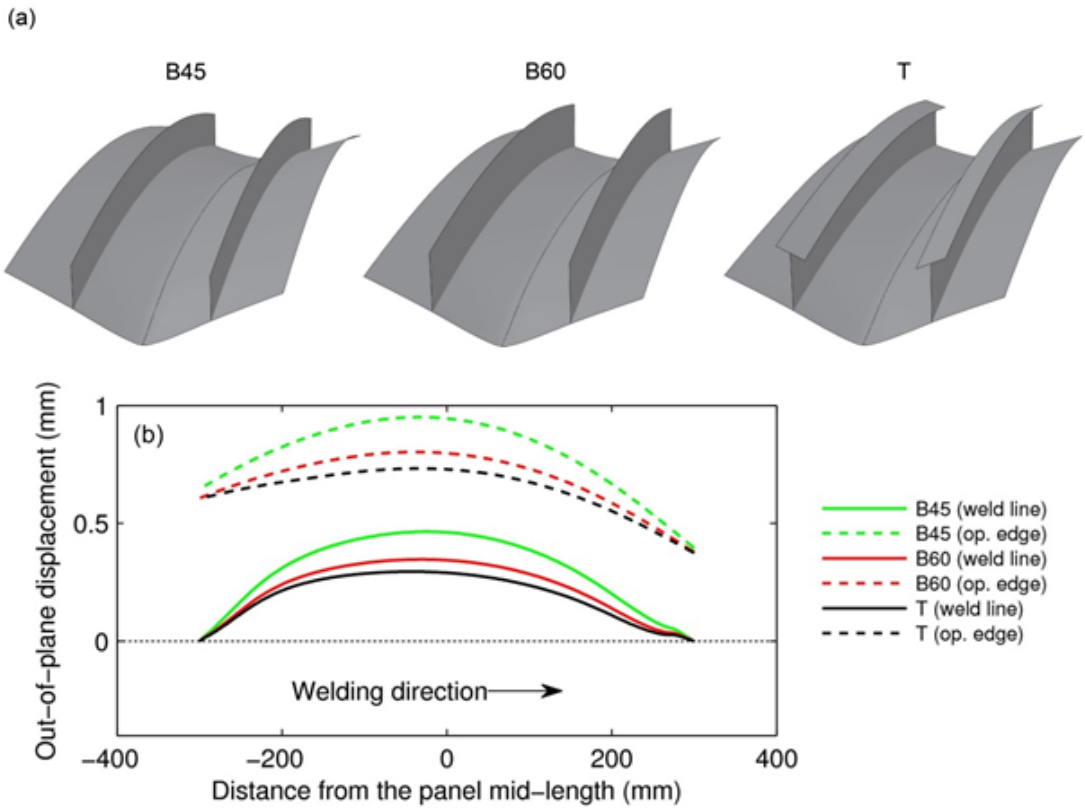

Figure 14: Distortion of the panels in the end of the FSW simulation: (a) Deformed shapes (symmetry plane on weld line; displacements amplified 50 times along *Oy*) and (b) Corresponding displacements at the end of the FSW simulation along the weld line and the opposite edge.

4. Conclusions

Taking into account the most distinctive features of the proposed model, the following conclusions and summary can be drawn:

- A shell-based finite element model was developed to simulate the transient thermal field and stress-strain distribution in a friction stir welding process;
- The numerical model was calibrated assuming a relatively simple benchmark, consisting of single plates joining by means of FSW process, used to validate residual stresses and mechanical properties variations by comparison with experimental data;

- The validated model was applied to simulate an industrial application dealing with the friction stir welding of integrally stiffened panels aiming to predict the welding effects in terms of residual stresses and distortions;
- Three different single stiffener cross-section geometries were considered in the analyses: a panel with a T stiffener geometry (panel T) and other two panel geometries consist in a variation of the previous one, with blade stiffeners (panel B45 and panel B60).
- The residual stresses distribution results were quite similar for the different panels, except in the stiffeners zone.
- The distortion magnitude was also similar in terms of shape pattern but different in terms of magnitude, comparing results for panels with distinct cross-sections.

Following the achievements presented in this contribution, and using as a design tool the developed modelling and numerical simulation framework, the next steps of the authors will be the analysis and structural characterization of the behaviour of friction stir welded stiffened panels when subjected to buckling loads. In particular, the influences of the joining processes on the compressive limit loads achieved by those panels will be investigated.

Acknowledgements

The authors wish to acknowledge the support given by *Fundação para a Ciência e a Tecnologia, Ministério para a Educação e Ciência*, Portugal, under the grants PTDC/EME-PME/113835/2009 and SFRH/BD/82456/2011.

References

[1] A. Alberg, M. Langseth, P.K. Larsen, Stiffened aluminium panels subjected to axial compression, Thin-Walled Structures **39** (2001) 861-885.

[2] R.S. Mishra, Z.Y. Maba, Friction stir welding and processing, Materials Science and Engineering R **50** (2005), 1–78.

[3] G. Pouget, A.P. Reynolds, Residual stress and microstructure effects on fatigue crack growth in AA2050 friction stir welds, International Journal of Fatigue **30** (2008) 463–472.

[4] B.T. Gibson, D.H. Lammlein, T.J. Prater, W.R. Longhurst, C.D Cox, M.C. Ballun, K.J. Dharmaraj, G.E. Cook, A.M. Strauss, Friction stir welding: Process, automation, and control, Journal of Manufacturing Processes **16** (2014) 56–73.

[5] S. Zimmer, L. Langlois, J. Laye, R. Bigot, Experimental investigation of the influence of the FSW plunge processing parameters on the maximum generated force and torque, International Journal of Advanced Manufacturing Technology **47** (2010) 201-215.

[6] A. Murphy, W. McCune, D. Quinn, M. Price, The characterisation of friction stir welding process effects on stiffened panel buckling performance, Thin-Walled Structures **45** (2007) 339–51.

[7] A. Murphy, M. Price, R. Curran, Integration of strength and process modelling of friction-stir-welded fuselage panels, Journal of Aerospace Computing, Information and Communication, **3** (2006) 159–176.

[8] G. Buffa, L. Fratini, G. Marannano, A. Pasta, Effect of the mutual position between weld seam and reinforcement on the residual stress distribution in Friction Stir Welding of AA6082 skin and stringer structures, Thin-Walled Structures **103** (2016) 62–71.

[9] ABAQUS, Abaqus Documentation (v.6.14). Simulia Dassault Systémes (2014).

[10] D. Quinn, A. Murphy, W. McEwan, F. Lemaitre, Stiffened panel stability behaviour and performance gains with plate prismatic sub-stiffening, Thin-Walled Structures **47** (2009) 1457-1468.

[11] C. Lynch, A. Murphy, M. Price, A. Gibson, The computational post buckling analyses of fuselage stiffened panels loaded in compression, Thin-Walled Structures **42** (2004) 1445-1464.

[12] J. Campbell, L. Hetey, R. Vignjevic, Non-linear idealisation error analysis of a metallic stiffened panel loaded in compression, Thin-Walled Structures **54** (2012) 44-53.

[13] J.F. Caseiro, R.A.F. Valente, A. Andrade-Campos, J.W. Yoon, Elasto-plastic buckling of integrally stiffened panels (ISP): An optimization approach for the design of cross-section profiles, Thin-Walled Structures **49** (2011) 864-873.

[14] J.F. Caseiro, R.A.F. Valente, A. Andrade-Campos, J.W. Yoon, On the elasto-plastic buckling of Integrally Stiffened Panels (ISP) joined by Friction Stir Welding (FSW): Numerical simulation and optimization algorithms, International Journal of Mechanical Sciences **76** (2013) 49-59.

[15] F. Al-Badour, N. Merah, A. Shuaib, A. Bazoune, Coupled Eulerian Lagrangian finite element modelling of friction stir welding processes, Journal of Materials Processing Technology **213** (2013) 1433–1439.

[16] W.A. Wall, M. Bischoff, K.U. Bletzinger, E. Ramm, Models and Finite Elements for Thin-walled Structures, in: Erwin Stein, René de Borst and Thomas J.R. Hughes (Eds.), Encyclopedia of Computational Mechanics, Volume 2: Solids, Structures and Coupled Problems, John Wiley & Sons, 2004, pp. 1-25.

[17] R.M.F. Paulo, P. Carlone, R.A.F. Valente, F. Teixeira-Dias, G.S. Palazzo, Numerical simulation of AA2024-T3 friction stir welding (FSW) process: Sensitivity analyses and influence of decisions during modelling stages, Key Engineering Materials **651-653** (2015) 919-924.

[18] P. Carlone, G.S. Palazzo, Influence of process parameters on microstructure and mechanical properties in AA2024-T3 friction stir welding, Metallogaphy Microstrucure and Analysis **2** (2013) 213-222.

[19] P. Carlone, G. Palazzo, Longitudinal Residual Stress Analysis in AA2024-T3 Friction Stir Welding, The Open Mechanical Engineering Journal **7** (2013) 18-26.

[20] M.B. Prime, Cross-sectional mapping of residual stresses by measuring the surface contour after a cut, Journal of Engineering Materials and Technology **123** (2001) 162-168.

[21] R.M.F. Paulo, P. Carlone, R.A.F. Valente, F. Teixeira-Dias, G.S. Palazzo, Influence of friction stir welding residual stresses on the compressive strength of aluminium alloy plates, Thin-Walled Structures **74** (2014) 184–190.

[22] M.R. Sonne, C.C. Tutum, J.H. Hattel, A. Simar, B. de Meester, The effect of hardening laws and thermal softening on modeling residual stresses in FSW of aluminium alloy 2024-T3, Journal of Materials Processing Technology **213** (2013) 477-486.

[23] Aerospace Specification Metals Inc., <asm.matweb.com> (March, 2012).

[24] R.V. Preston, H.R. Shercliff, P.J. Withers, S. Smith, Physically-based constitutive modelling of residual stress development in welding of aluminium alloy 2024, Acta Materialia **52** (2004) 4973-4983.

[25] R.M.F. Paulo, P. Carlone, R. Valente, F. Teixeira-Dias, G.S. Palazzo, Buckling analysis of aluminium alloy structures accounting for friction stir welding effect, Proceedings of the Ninth International Conference on Engineering Computational Technology, P. Iványi, B.H.V. Topping (Eds.), Naples, 2014.

[26] M.R. Sonne, P. Carlone, G.S. Palazzo, J.H. Hattel, Numerical modeling of AA2024-T3 friction stir welding process for residual stress evaluation, including softening effects, Key Engineering Materials **611-612** (2014) 1675-1682.

[27] D.G. Richards, P.B. Prangnell, S.W. Williams, P.J. Withers, Global mechanical tensioning for the management of residual stresses in welds, Materials Science and Engineering A **489** (2008) 351-362.

[28] D.G. Richards, P.B. Prangnell, P.J. Withers, S.W. Williams, T. Nagy, S. Morgan, Efficacy of active cooling for controlling residual stresses in friction stir welds, Science and Technology of Welding and Joining **15** (2010) 156-165.

[29] A. Bastier, M.H. Maitournam, F. Roger, K. Dang Van, Modelling of the residual state of friction stir welded plates, Journal of Materials Processing Technology **200** (2008) 25-37.

[30] Z. Feng, X.L. Wang, S.A. David, P.S. Sklad, Modelling of residual stresses and property distributions in friction stir welds of aluminium alloy 6061-T6, Science and Technology of Welding and Joining **12** (2007) 348-356.

[31] O.R. Myhr, Ø. Grong, Process modelling applied to 6082-T6 aluminium weldments - I. Reaction kinetics, Acta Metallurgica et Materialia **39** (1991) 2693-2702.

[32] R.W. McCune, A. Murphy, M. Price, J. Butterfield, The influence of friction stir welding idealization on residual stress and distorsion predictions for future airflame assembly simulations, Journal of Manufacturing Science and Engineering **134** (2012).

[33] A.J. Leonard, Microstructure and ageing behaviour of FSWs in aluminium alloys 2014A-T651 and 7075-T651, Proceedings of the 2nd International Symposium on 'Friction Stir Welding', Gothenburg (2000).

[34] C.B. Fuller, M.W. Mahoney, M. Calabrese, L. Micona, Evolution of microstructure and mechanical properties in naturally aged 7050 and 7075 Al friction stir welds, Materials Science and Engineering: A **527** (2010) 2233-2240.

[35] A. Pastor, H.G. Svoboda, Time-evolution of Heat Affected Zone (HAZ) of Friction Stir Welds of AA7075-T651, Journal of Materials Physics and Chemistry **1** (2013) 58-64.

[36] M.Z.H. Khandkar, J.A. Khan, A.P. Reynolds, M.A. Sutton, Predicting residual thermal stresses in friction stir welded metals, Journal of Materials Processing Technology **174** (2006) 195-203.

[37] H. Schmidt, J. Hattel, A local model for the thermomechanical conditions in friction stir welding, Modelling and Simulation in Materials Science and Engineering **13** (2005) 77-93.

[38] J.W. Yoon, G.H. Bray, R.A.F. Valente, T.E.R. Childs, Buckling analysis for an integrally stiffened panel structure with a friction stir weld, Thin-Walled Structures **47** (2009) 1608-1622.

[39] D. Yan, A. Wu, J. Silvanus, Q. Shi, Predicting residual distortion of aluminium alloy stiffened sheet after friction stir welding by numerical simulation, Materials and Design **32** (2011) 2284-2291.

[40] Q.Y. Shi, J. Silvanus, Y. Liu, D.Y. Yan, H.K. Li, Experimental study on distortion of Al-6013 plate after friction stir welding, Science and Technology of Welding and Joining **13** (2008) 472-478.